

AD-A170 029
G
H T G

AFOSR-TR. 86 - 0342

2

Annual Scientific Report
on
FUNDAMENTAL PROCESSES IN PARTIALLY IONIZED PLASMAS
Grant AFOSR-83-0108

Prepared for
AIR FORCE OFFICE OF SCIENTIFIC RESEARCH
For the Period
February 1, 1985 to January 31, 1986

DTIC
ELECTE
JUL 23 1986
B

Approved for public release;
distribution unlimited.

Submitted by
C. H. Kruger, Principal Investigator
M. Mitchner, Co-Principal Investigator
S. A. Self, Co-Principal Investigator

HIGH TEMPERATURE GASDYNAMICS LABORATORY
Mechanical Engineering Department
Stanford University

DTIC FILE COPY

Annual Scientific Report
on
FUNDAMENTAL PROCESSES IN PARTIALLY IONIZED PLASMAS
Grant AFOSR-83-0108

Prepared for
AIR FORCE OFFICE OF SCIENTIFIC RESEARCH

For the Period
February 1, 1985 to January 31, 1986

AIR FORCE OFFICE OF SCIENTIFIC RESEARCH (AFOSR)
NOTICE OF REVISIONS
This report is approved for distribution as indicated on the cover page.
Distribution is limited to AFOSR and AFOSR-83-0108.
MATTHEW J. KRUGER
Chief, Technical Information Division

Submitted by
C. H. Kruger, Principal Investigator
M. Mitchner, Co-Principal Investigator
S. A. Self, Co-Principal Investigator

UNCLASSIFIED

ADA 170029

SECURITY CLASSIFICATION OF THIS PAGE

REPORT DOCUMENTATION PAGE

1a. REPORT SECURITY CLASSIFICATION Unclassified			1b. RESTRICTIVE MARKINGS None			
2a. SECURITY CLASSIFICATION AUTHORITY			Approved for public release; distribution unlimited.			
2b. DECLASSIFICATION/DOWNGRADING SCHEDULE						
4. PERFORMING ORGANIZATION REPORT NUMBER(S)			5. MONITORING ORGANIZATION REPORT NUMBER(S)			
6a. NAME OF PERFORMING ORGANIZATION Stanford University		6b. OFFICE SYMBOL (If applicable)	7a. NAME OF MONITORING ORGANIZATION Air Force Office of Scientific Research			
6c. ADDRESS (City, State and ZIP Code) Department of Mechanical Engineering Stanford, California 94305-3030			7b. ADDRESS (City, State and ZIP Code) Directorate of Physical & Geo. Sci., AFOSR/NP Bolling AFB, Building 410 Washington, D.C. 20332			
8a. NAME OF FUNDING/SPONSORING ORGANIZATION Air Force Office of Scientific Research		8b. OFFICE SYMBOL (If applicable) NP	9. PROCUREMENT INSTRUMENT IDENTIFICATION NUMBER Grant AFOSR-83-0108			
8c. ADDRESS (City, State and ZIP Code) Directorate of Physical & Geo Sci. AFOSR/NP, Bolling AFB, Bldg. 410 Washington, D.C. 20332			10. SOURCE OF FUNDING NOS.			
11. TITLE (Include Security Classification) Fundamental Processes in Partially Ionized Plasmas			PROGRAM ELEMENT NO. 61102F	PROJECT NO. 2301	TASK NO. A7	WORK UNIT NO. N/A
			12. PERSONAL AUTHOR(S) C.H. Kruger, PI. M. Mitchner, Co-PI. S.A. Self, Co-PI			
13a. TYPE OF REPORT Annual Scientific Rpt		13b. TIME COVERED FROM 2/1/85 TO 1/31/86	14. DATE OF REPORT (Yr., Mo., Day) February 28, 1986		15. PAGE COUNT 77	
16. SUPPLEMENTARY NOTATION						
17. COSATI CODES			18. SUBJECT TERMS (Continue on reverse if necessary and identify by block number)			
FIELD	GROUP	SUB. GR.	Plasma	Sheath	Secondary Flow Power	Cathode
			Recombination	Boundary layer	Diagnostics	Anode Discharge
			Three-body	MHD	Electrothermal	Breakdown
19. ABSTRACT (Continue on reverse if necessary and identify by block number) This report describes progress during the third year of a research program on the Fundamental Processes in Partially Ionized Plasmas conducted in the High Temperature Gasdynamics Laboratory at Stanford University. This research is directed to three major areas: recombination in molecular plasmas, discharge effects (plasma electrode interaction) and interaction of discharges and fluid dynamics. Recombination and ionization are fundamental processes that play a role in nearly all applications and natural phenomena that involve partially ionized plasmas. Under the present program, experiments have been designed and theoretical analyses conducted to obtain a better knowledge of the rates of electron recombination in the presence of molecular species. Studies are continuing of the near-electrode region and the processes by which current is transferred between the plasmas and the electrodes. The first stage of theoretical modeling of these processes has now been completed and published. A study of the interaction of discharges and fluid dynamics has measured the significant secondary flows caused by the interaction of a magnetic field with a current-carrying plasma.						
20. DISTRIBUTION/AVAILABILITY OF ABSTRACT UNCLASSIFIED/UNLIMITED <input checked="" type="checkbox"/> SAME AS RPT <input type="checkbox"/> DTIC USERS <input type="checkbox"/>			21. ABSTRACT SECURITY CLASSIFICATION Unclassified			
22a. NAME OF RESPONSIBLE INDIVIDUAL Bruce L. Smith			22b. TELEPHONE NUMBER (Include Area Code) (202) 767 4900		22c. OFFICE SYMBOL NH	

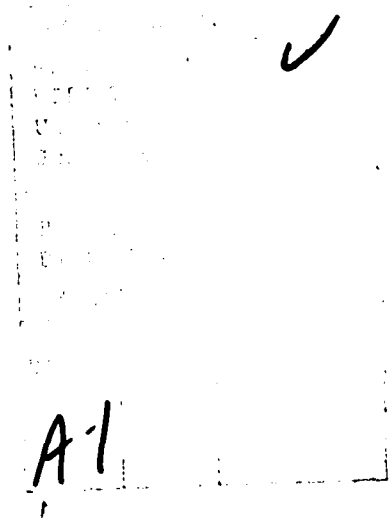
Block 19 (Abstract)

Measurements have been made of secondary flows, and of their effects on profiles of axial velocity, turbulence intensity and electrical conductivity. Experimental and theoretical research in each of these areas is continuing.

SECRET

Table of Contents

<u>Section</u>	<u>Page</u>
1.0 INTRODUCTION.....	1
2.0 PROJECT SUMMARIES.....	3
2.1 Recombination in Molecular Plasmas.....	3
2.2 Discharge Effects: Plasma-Electrode Interaction.....	30
2.3 Interaction of Discharges and Fluid Dynamics.....	48
3.0 REFERENCES.....	71
4.0 PUBLICATIONS AND PRESENTATIONS.....	75
5.0 PERSONNEL.....	77



1.0 INTRODUCTION

This report describes progress during the third year of a research program on the Fundamental Processes in Partially Ionized Plasmas conducted in the High Temperature Gasdynamics Laboratory at Stanford University. This research is supported by a grant from the Air Force Office of Scientific Research (AFOSR-83-0108) and is conducted under the direction of Professors Charles H. Kruger, Morton Mitchner, and Sidney Self. Three Ph.D. candidates are currently conducting their doctoral research under this program.

Several space power and propulsion systems of potential long-range interest to the Air Force involve partially ionized plasmas. Such systems include MPD thrusters, both open and closed cycle MHD power, and thermionic energy conversion. Although the specific configurations, the exact operating conditions, and which of the competing systems will prove to be most useful in the long term remain to be established, it is important at this time to provide a broad fundamental research base in support of development activity. In particular, there are a number of key issues regarding the properties and discharge behavior of partially ionized plasmas and the interaction of discharges with fluid dynamics that need to be understood before the potential and limitations of competing systems can be fully evaluated. In addition, it is important that outstanding young applied scientists be educated in these areas.

The present research on partially ionized plasmas is discipline rather than device oriented and is currently focused on three major areas:

1. Recombination in molecular plasmas
2. Discharge effects: plasma electrode interaction
3. Interaction of discharges and fluid dynamics

In addition, each of these areas involves the development and application of modern plasma diagnostic techniques.

These areas are overlapping and mutually supportive. Thus, understanding of plasma properties is important to the study of discharges and their interaction with fluid dynamics. In the same spirit, we are interested in the development of plasma diagnostics so that they can be applied in our research objectives. In each area, the research is primarily experimental in nature, with supporting theoretical studies for the planning of the research and interpretation of the data.

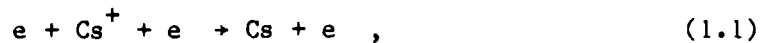
Progress during the third year in each of the three research areas is described by means of Project Summaries in Section 2.0.

Publications and Presentations resulting from this work are cited in Section 4.0, and Section 5.0 lists the personnel who have contributed to this report.

2.1 Recombination in Molecular Plasmas

Introduction

In applications of interest to the Air Force (e.g. MHD generators and space propulsion) where a high pressure (i.e. of the order of an atmosphere) partially-ionized plasma flows past a cooled surface, recombination of electrons occurs with positive alkali-metal ions (such as Cs^+) under conditions for which there have been few, if any, reported measurements of the recombination rate. Typically, these conditions are for relatively low electron number densities n_e where the three-body recombination process



usually dominant at higher electron number densities (e.g. $n_e \gtrsim 10^{12} \text{ cm}^{-3}$, at $T \gtrsim 1000 \text{ K}$), no longer plays a major role.

To obtain an improved understanding of recombination processes under such conditions, we have proposed to design and perform experiments in which a highly nonequilibrium plasma is produced in a mixture containing cesium vapor and nitrogen gas. From an engineering point-of-view, it is the actual value of the recombination rate which is of primary importance, independent of what the underlying kinetic mechanisms may be. However a knowledge of the mechanisms is very useful in that it enables one to extrapolate and predict values of the recombination rate for conditions that go beyond those for which measurements exist.

In addition to measurements of the recombination rates, another objective of our proposed work is therefore to identify the operative recombination mechanisms and to make comparisons of our measurements with existing theories. In previous descriptions of our proposed work, we have discussed the three-body recombination process



as one that would occur under conditions of interest (e.g. a MHD boundary layer). The recombination coefficient for this reaction has been

calculated by Bates et al. [1.3], but no experiments have been performed to date that would enable a comparison to be made with theory.

One experimental arrangement for producing the nonequilibrium conditions which are necessary to study recombination is to employ a supersonic nozzle to rapidly expand a flowing high temperature plasma, consisting of N_2 and thermally ionized Cs. Measurements of the electron number density before and after the expansion would be compared with calculated values obtained from the electron continuity equation. Since the calculated values of n_e depend on the recombination coefficient $\alpha_{N_2}(T)$, such an experiment would provide a means for inferring the recombination rate. (Here α is defined for recombining conditions by the relation $dn_e/dt = -\alpha n_e n_i$, where n_i denotes the number density of the ions with which the electrons are recombining.)

To analyze more accurately the feasibility of such an experiment, a mathematical model of the flow was formulated, and solved numerically. The results showed that in order for the value of n_e at the exit of the nozzle to depart significantly from its frozen value, the upstream value of n_e would need to be sufficiently large that the process (1.1) would contribute appreciably to the over-all recombination rate. Thus the accuracy with which α_{N_2} could be determined would be reduced. This kind of an experiment also has the disadvantage that the recombination would be occurring under non-isothermal conditions, thereby further complicating the reduction of the data.

Because of these limitations (as well as others) effort has been directed toward analyzing alternative experimental arrangements for producing the required nonequilibrium conditions. Among the alternatives considered, the approach that appeared most attractive was one in which the ionizational nonequilibrium would be achieved by pulsed photoionization of Cs vapor confined with N_2 in a heated test cell. The recombination coefficient $\alpha_{N_2}(T)$ would be determined by measuring the decay of n_e as a function of time, following the completion of the photoionization pulse. In a photoionization experiment the recombination is non-steady in time and uniform in space, in contrast to a rapid expansion experiment which is steady in time and nonuniform in space.

In the remainder of this section, we outline first our research objectives and then discuss the present status of the research. During the past year a theoretical analysis directed toward showing in more detail the feasibility of a pulsed photoionization experiment was completed, and substantial progress was made toward completion of the experimental facility. The main result of our present feasibility study is to show that for mixtures of interest, below a temperature of about 800K, recombination involves several ion-molecule reactions proceeding simultaneously. (See the Feb. 1, 1985 to Jan. 31, 1985 Annual Scientific Report for a description of past feasibility calculations.) However for temperatures in excess of about 1000K, electron recombination is dominated by the three-body process (1.2). Our recombination rate measurements at higher temperatures should therefore enable us to make comparisons with the Bates theory. Also during the past year much of the experimental facility has been fabricated. Items completed include the reaction cell, the heating and vacuum system, and a prototype flash lamp power supply.

Research Objectives

1. To design and construct an experimental system that can produce a recombining alkali metal plasma under conditions where the molecular three-body process dominates.
2. To examine, in particular, the recombination of cesium ions in the presence of nitrogen.
3. To measure the desired recombination rate as a function of the background gas temperature.
4. To measure the recombination rate as a function of various values of the partial pressures of Cs and N₂.

5. To examine the recombination rate of interest in a mixture of molecular species.
6. To design and construct a suitable pulse forming circuit for a high intensity flashlamp and to explore the use of pulsed photoionization as a means for producing the desired plasma conditions.
7. To determine the electron number density as a function of time in a plasma afterglow, and to deduce the recombination rate from this measurement.
8. To develop a four pin probe for measuring the time resolved plasma electrical conductivity as a diagnostic for determining the electron concentration.
9. To develop a method employing an equilibrium plasma for calibrating the electron conductivity probe.
10. To examine the possible use of optical diagnostic methods such as measurement of the emission of free-bound continuum radiation, as a means for obtaining a check on the data via an independent, redundant procedure.
11. To assess the possible roles of the presence of the dimer ions Cs_2^+ and ion clusters such as $\text{Cs}^+\cdot\text{N}_2$ and $\text{Cs}^+\cdot\text{H}_2\text{O}$ (the water vapor will be present in small quantities as an impurity) in contributing to the measured recombination rates.

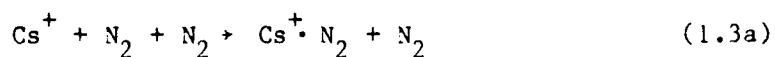
Status of Research

During the period February 1985 through January 1986 research progress consisted primarily of the development of a detailed computer model of the reaction kinetics for the pulsed photoionization experiment, and of the construction and assembly of major elements of the experimental facility. The model includes important ion-molecule

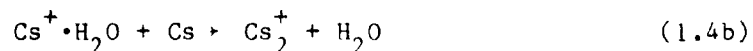
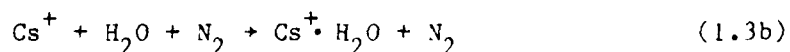
chemistry, and it demonstrates the validity of electron loss measurements as a means for determining the rate of reaction (1.2). A reaction cell, three zonal ovens, a temperature measurement system, a temperature control system, and a vacuum system were all completed during the past year. Additionally, a flashlamp power supply was prototyped.

Reaction Kinetics Model

In previous discussions we have demonstrated that experimental conditions can be chosen such that recombination by process (1.2) would dominate that by process (1.1). In addition to process (1.2), a loss of electrons under conditions of interest could also occur through a sequence of reactions involving fast formation of the ion cluster $Cs^+ \cdot N_2$, fast 2-body switching to form Cs_2^+ , followed by dissociative recombination of the cesium dimer ion. These processes can be written as follows:



Reactions analogous to (1.3a) and (1.4a) can occur when water vapor impurities are present and H_2O replaces N_2 as a clustering partner. These reactions are written:



Other possible mechanisms of electron loss are electron dissociative recombination with $Cs^+ \cdot N_2$, electron attachment, and ion-ion recombination as represented respectively by the reactions





In what follows, we present a detailed examination of the overall recombination process that includes both the ion-molecule reaction channel (1.3), (1.4), and (1.5) as well as the three-body processes (1.1 and 1.2). Using estimates of the recombination rate coefficients and equilibrium constants (to calculate the backward rates) constructed from available information in the literature (see Table 1.1 for references), we show that experimental conditions at higher temperatures can be chosen to maintain process (1.2) as the dominant electron loss mechanism, despite the fast reactions (1.3) and (1.4). Later we show that inclusion of reactions (1.6)-(1.8) does not affect the dominance of reaction (1.2) in electron loss frequency. In addition we also show that by using a liquid nitrogen cold trap and because of the gettering action of Cs, as well as from considerations of the reaction kinetics, the deleterious effects of a possible water impurity are not significant.

Partial Equilibrium

Although reactions (1.3) and (1.4) proceed in a forward direction rapidly relative to the three other reactions considered, the backward rates for these reactions are also large. Reactions (1.3) and (1.4) are able to quickly reach a partial equilibrium condition where the forward and backward rate are equal in magnitude. This partial equilibrium is maintained while the recombination reactions slowly change the ion and electron concentrations.

Table 1.1 lists the preceding ten chemical reactions. Also listed are the values of the corresponding forward and backward rate constants and the ratios of these two constants (i.e., the equilibrium constants), used in all subsequent calculations. The constants were obtained using the references shown. The photoionization of Cs vapor by ultraviolet radiation from a flashlamp can be represented by the reaction

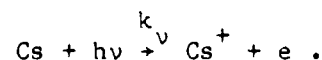


Table 1.1 Reaction Rate and Equilibrium Constants

Reaction	Constants	References
$e + Cs^+ + e \xrightleftharpoons[k_{-1}]{k_1} Cs + e$	$k_1 = 1.09 \times 10^{-8} / T^{4.5} \text{ cm}^6/\text{s}$ $k_{-1} = 2.64 \times 10^7 / T^3 \exp(-45128/T) \text{ cm}^3/\text{s}$ $k_1/k_{-1} = 4.13 \times 10^{-16} T^{-1.5} \exp(45128/T) \text{ cm}^3$	1.9, 1.1
$e + Cs^+ + N_2 \xrightleftharpoons[k_{-2}]{k_2} Cs + N_2$	$k_2 = 6.58 \times 10^{-29} \exp(590.4/T) \text{ cm}^6/\text{s}$ $k_{-2} = 1.59 \times 10^{-13} T^{1.5} \exp(-44538/T) \text{ cm}^3/\text{s}$ $k_2/k_{-2} = 4.13 \times 10^{-16} T^{-1.5} \exp(45128/T) \text{ cm}^3$	1.3, 1.1
$Cs^+ + N_2 + N_2 \xrightleftharpoons[k_{-3a}]{k_{3a}} Cs^+ \cdot N_2 + N_2$	$k_{3a} = 6.42 \times 10^{-10} \text{ cm}^3/\text{s}$ $k_{-3a} = 7.81 \times 10^{18} T^{-1.5} \exp(-3374/T) \text{ s}^{-1}$ $k_{3a}/k_{-3a} = 8.22 \times 10^{-29} T^{1.5} \exp(3374/T) \text{ cm}^3$	1.15, 1.16, 1.18 1.10, 1.11, 1.12 1.7, 1.22, 1.14
$Cs^+ + H_2O + N_2 \xrightleftharpoons[k_{-3b}]{k_{3b}} Cs^+ \cdot H_2O + N_2$	$k_{3b} = 6.42 \times 10^{-10} \text{ cm}^3/\text{s}$ $k_{-3b} = 2.44 \times 10^{18} / T \exp(-7049/T) \text{ s}^{-1}$ $k_{3b}/k_{-3b} = 2.63 \times 10^{-28} T \exp(7049/T) \text{ cm}^3$	1.16, 1.8, 1.18
$Cs^+ \cdot N_2 + Cs \xrightleftharpoons[k_{-4a}]{k_{4a}} Cs_2^+ + N_2$	$k_{4a} = 10^{-9} \text{ cm}^3/\text{s}$ $k_{-4a} = \exp(-1.081 \times 10^4 / T - 23.97 + 8.303 \times 10^{-4} T - 1.496 \times 10^{-7} T^2) \text{ cm}^3/\text{s}$ $k_{4a}/k_{-4a} = \exp(1.081 \times 10^4 / T + 3.244 - 8.303 \times 10^{-4} T + 1.496 \times 10^{-7} T^2)$	1.17, 1.19, 1.20
$Cs^+ \cdot H_2O + Cs \xrightleftharpoons[k_{-4b}]{k_{4b}} Cs_2^+ + H_2O$	$k_{4b} = 10^{-9} \text{ cm}^3/\text{s}$ $k_{-4b} = \exp(-7.134 \times 10^3 / T - 23.39 + 8.525 \times 10^{-4} T - 1.559 \times 10^{-7} T^2) \text{ cm}^3/\text{s}$ $k_{4b}/k_{-4b} = \exp(7.134 \times 10^3 / T + 2.668 - 8.525 \times 10^{-4} T + 1.559 \times 10^{-7} T^2)$	1.17, 1.19, 1.20

Table 1.1 Reaction Rate and Equilibrium Constants (continued)

Reaction	Constants	References
$e + \text{Cs}_2 \xrightleftharpoons[k_{-5}]{k_5} \text{Cs} + \text{Cs}$	$k_5 = 10^{-8} * (300/T)^{1/2} \text{ cm}^3/\text{s}$ $k_{-5} = \exp(-3.094 \times 10^4/T + 2.5 \ln(T) - 41.57 - 8.303 \times 10^{-4} * T + 1.496 \times 10^{-7} * T^2) \text{ cm}^3/\text{s}$ $k_5/k_{-5} = \exp(3.094 \times 10^4/T - 3 \ln(T) + 26.00 + 8.303 \times 10^{-4} * T - 1.496 \times 10^{-7} * T^2)$	1.21, 1.22
$e + \text{Cs}^+ \cdot \text{N}_2 \xrightleftharpoons[k_{-6}]{k_6} \text{Cs} + \text{N}_2$	$k_6 = 5.0 \times 10^{-7} * (300.0/T)^{1.5} \text{ cm}^3/\text{s}$ $k_{-6} = 5.2 \times 10^{-16} * T^{1.5} * \exp(-41754./T) \text{ cm}^3/\text{s}$ $k_6/k_{-6} = 5.02 \times 10^{12} * T^{-3} * \exp(41754./T)$	1.22
$e + \text{Cs} + \text{N}_2 \xrightleftharpoons[k_{-7}]{k_7} \text{Cs}^- + \text{N}_2$	$k_7 = 8.2 \times 10^{-14} \text{ cm}^3/\text{s}$ $k_{-7} = 1.98 \times 10^2 * T^{1.5} * \exp(-5452.1/T) \text{ 1/s}$ $k_7/k_{-7} = 4.14 \times 10^{-16} * T^{-1.5} * \exp(5452.1/T) \text{ cm}^3$	1.31
$\text{Cs}^- + \text{Cs}^+ \xrightleftharpoons[k_{-8}]{k_8} \text{Cs} + \text{Cs}$	$k_8 = 2.0 \times 10^{-7} * 300/T \text{ cm}^3/\text{s}$ $k_{-8} = 2.0 \times 10^{-7} * 300/T * \exp(-39673/T) \text{ cm}^3/\text{s}$ $k_8/k_{-8} = \exp(39673/T)$	1.11, 1.32, 1.33

The photon flux is modeled as a rectangular function in time, and the Cs vapor can be shown to be optically thin. Under these conditions the rate of increase of the electron number density can be represented by $d[e]/dt = [Cs]k_v$ where k_v is the integral over wavelength of the product of the photon flux and the total photoionization cross section. The value for k_v used in these calculations is 1.0 sec^{-1} . This value corresponds to a photon flux (wavelengths < 318 nm) of about 10^{20} photons/cm²·sec, which is an estimate of the flux attainable with our pulsed short arc flashlamp system.

Shown in Figs. 1.1a, 1.2a, and 1.3a are the time histories of the number densities of the species of interest for three different test cell temperatures. The $\text{Cs}^+ \cdot \text{H}_2\text{O}$ species occurs in concentrations which

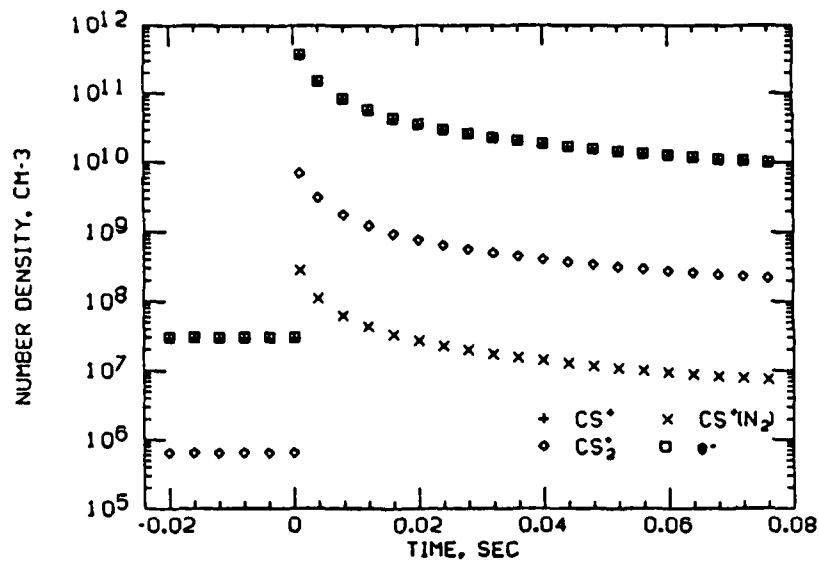


Fig. 1.1a Species concentrations from numerical solution of kinetics equations for reactions (1)-(5). $T=1000$ K; $[Cs]=4.5 \times 10^{14}$ cm^{-3} ; $[N_2]=10^{19}$ cm^{-3} ; $[H_2O]=10^{13}$ cm^{-3} . Two distinct regimes are shown: $t < 0$, complete equilibrium; $t > 1$ ms, plasma relaxation. Photoionization occurs between these regimes.

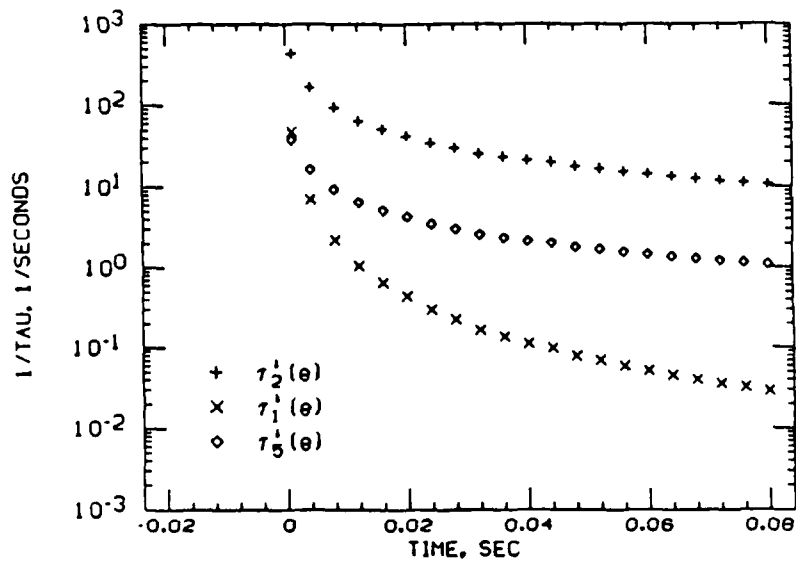


Fig. 1.1b Electron loss frequencies from numerical solution of kinetics equations for reactions (1)-(5). $T=1000$ K; $[Cs]=4.5 \times 10^{14}$ cm^{-3} ; $[N_2]=10^{19}$; $[H_2O]=10^{13}$ cm^{-3} . $1/\tau_1^+(e) \equiv (\text{net electron loss rate})/[e]$. For ambipolar diffusion, $1/\tau_{\text{diff}}^+(e) \lesssim 10$ sec^{-1} .

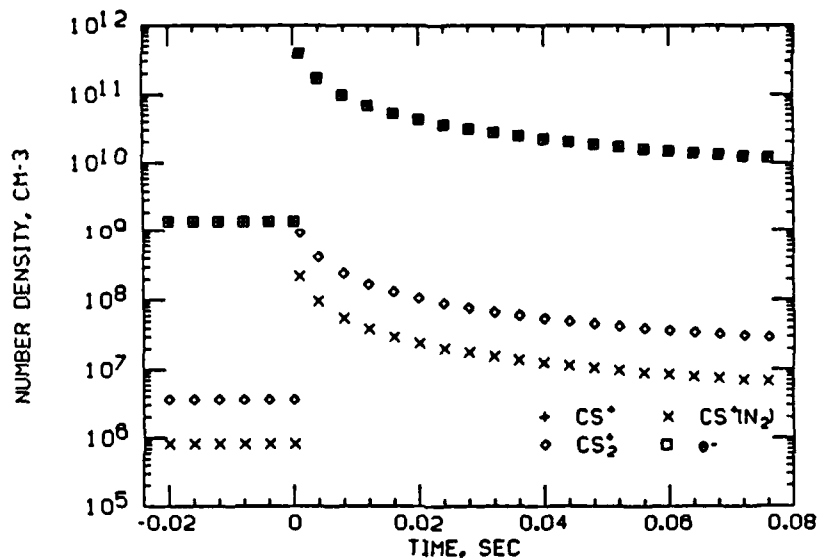


Fig. 1.2a Species concentrations from numerical solution of kinetics equations for reactions (1)-(5). $T=1200$ K; $[Cs]=4.5 \times 10^{14}$ cm^{-3} ; $[N_2]=10^{19}$ cm^{-3} ; $[H_2O]=10^{13}$ cm^{-3} . Two distinct regimes are shown: $t < 0$, complete equilibrium; $t > 1$ ms, plasma relaxation. Photoionization occurs between these regimes.

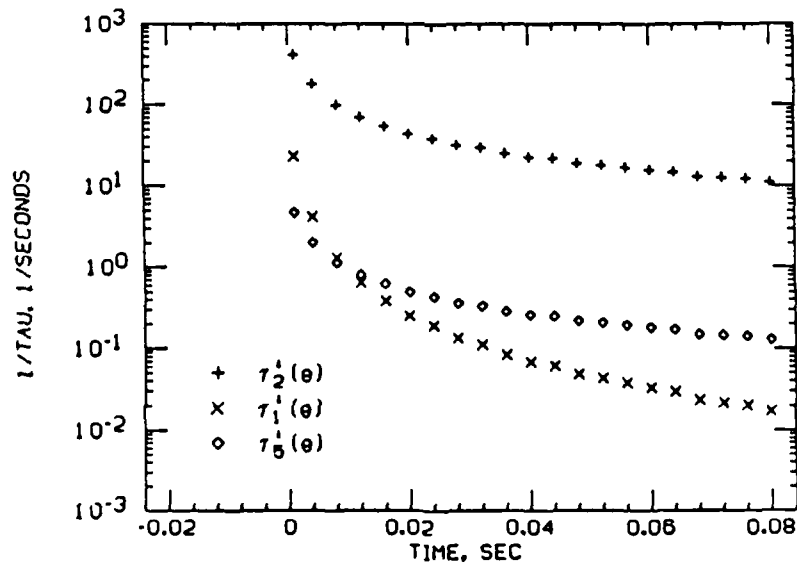


Fig. 1.2b Electron loss frequencies from numerical solution of kinetics equations for reactions (1)-(5). $T=1200$ K; $[Cs]=4.5 \times 10^{14}$ cm^{-3} ; $[N_2]=10^{19}$; $[H_2O]=10^{13}$ cm^{-3} . $1/\tau_1^+(e) \equiv (\text{net electron loss rate})/[e]$. For ambipolar diffusion, $1/\tau_{\text{diff}}^+(e) \lesssim 10$ sec^{-1} .

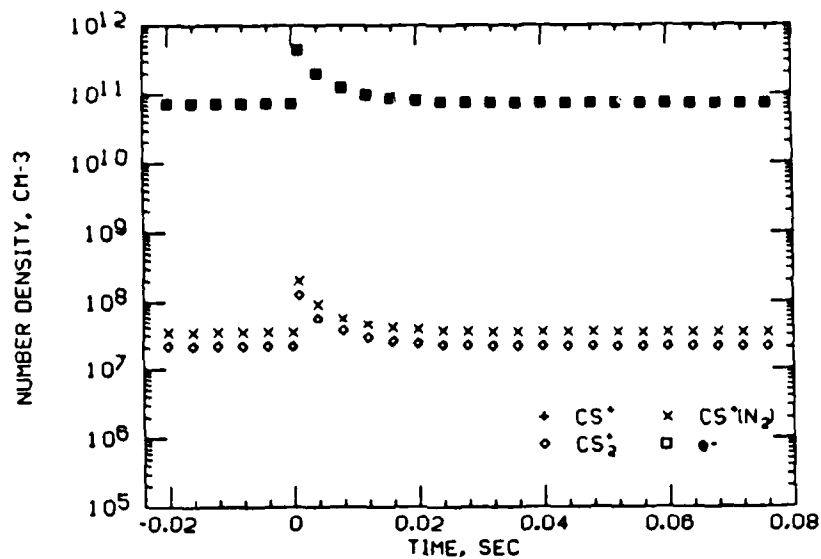


Fig. 1.3a Species concentrations from numerical solution of kinetics equations for reactions (1)-(5). $T=1500$ K; $[Cs]=4.5 \times 10^{14}$ cm^{-3} ; $[N_2]=10^{19}$ cm^{-3} ; $[H_2O]=10^{13}$ cm^{-3} . Two distinct regimes are shown: $t < 0$, complete equilibrium; $t > 1$ ms, plasma relaxation. Photoionization occurs between these regimes.

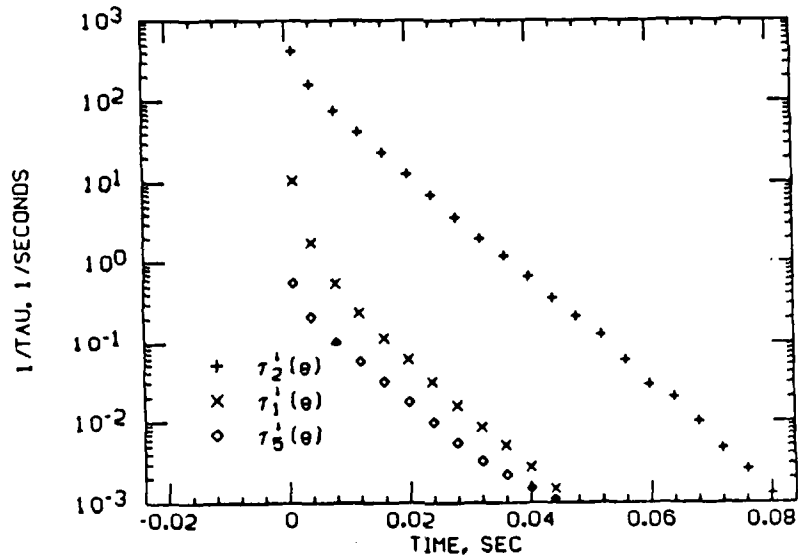
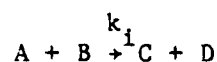


Fig. 1.3b Electron loss frequencies from numerical solution of kinetics equations for reactions (1)-(5). $T=1500$ K; $[Cs]=4.5 \times 10^{14}$ cm^{-3} ; $[N_2]=10^{19}$; $[H_2O]=10^{13}$ cm^{-3} . $1/\tau_i^+(e) \equiv (\text{net electron loss rate})/[e]$. For ambipolar diffusion, $1/\tau_{diff}^+(e) \lesssim 10$ sec^{-1} .

are off the lower end of the plotted scale. This species is treated explicitly in the section on impurities. (Note that reactions (1.6) - (1.8) are not modeled in the results presented in these figures.) It is assumed that the flash lamp is energized at $t=0$ and it is extinguished at $t=1$ ms; the dynamic relaxation of the nonequilibrium plasma occurs for times $t > 1$ ms. These plots were made by numerically solving the set of differential equations which describe the kinetics of the species involved in reactions (1.1) through (1.5). For $t < 0$, the plasma is in a state of local thermodynamic equilibrium. The equilibrium species concentrations shown in the figures are determined by the Cs vapor pressure (controlled by the reservoir temperature), by the initial N_2 concentration, and by the temperature of the reaction chamber. Typical values for these quantities were taken to be $[Cs]=4.5 \times 10^{14} \text{ cm}^{-3}$, $[N_2]=10^{19} \text{ cm}^{-3}$, $[H_2O]=10^{13} \text{ cm}^{-3}$, and $600 \text{ K} < T < 1500 \text{ K}$.

For a general reaction i where



we can obtain order of magnitude estimates of the characteristic times of significant decrease or increase of concentration of species respectively by, for example, $\tau_1^\downarrow(A) \sim (k_1[B])^{-1}$, or $\tau_1^\uparrow(C) \sim [C](k_1[A][B])^{-1}$. In what follows, it is shown how relations such as these may be employed to illustrate the essential physics underlying the numerical solutions presented in Figs. 1.1a, 1.2a, and 1.3a. Impurity reactions (1.3b) and (1.4b) have been included in the numerical solutions shown in Figs. 1.1-1.3, but an explanation of the effect of including these reactions is deferred until the section on impurities.

Using the equilibrium concentrations for $t < 0$ shown in Fig. 1.2a, characteristic times for significant changes in species concentrations are calculated in Table 1.2, for a temperature of 1200 K. Considering the important reactions affecting the electron concentration, the ordering $\tau_{\text{pulse}} = 10^{-3} \text{ sec.} \ll \tau_1^\downarrow < \tau_5^\downarrow < \tau_2^\downarrow$ demonstrates that the duration of the photoionization reaction (one millisecond) is sufficiently short to throw the plasma out of equilibrium. The recombination reactions

Table 1.2 Characteristic Times
 t=0, T=1200 K, Species concentrations from Fig. 1.2a

$\tau_{\text{pulse duration}} = 10^{-3}$ sec

$\tau_2^{\dagger}(e) = ([\text{Cs}^+] \cdot [\text{N}_2] \cdot k_2)^{-1} = (10^9 \cdot 10^{19} \cdot 10^{-28})^{-1} = 1$ sec

$\tau_5^{\dagger}(e) = ([\text{Cs}^+_{2}] \cdot k_5)^{-1} = (3 \times 10^6 \cdot 5 \times 10^{-9})^{-1} = 10^2$ sec

$\tau_1^{\dagger}(e) = ([\text{Cs}^+] \cdot [e] \cdot k_1)^{-1} = (10^9 \cdot 10^9 \cdot 10^{-22})^{-1} = 10^4$ sec

$\tau_{3a}^{\dagger}(\text{Cs}^+) = ([\text{N}_2] \cdot k_{3a})^{-1} = (10^{19} \cdot 6 \times 10^{-10})^{-1} = 10^{-9}$ sec

$\tau_2^{\dagger}(\text{Cs}^+) = ([e] \cdot [\text{N}_2] \cdot k_2)^{-1} = (10^9 \cdot 10^{19} \cdot 10^{-28})^{-1} = 1$ sec

$\tau_{4a}^{\dagger}(\text{Cs}^+_{2}) = [\text{Cs}^+_{2}] / ([\text{Cs}^+ \cdot \text{N}_2] \cdot [\text{Cs}] \cdot k_{4a}) =$
 $= 3 \times 10^6 / (8 \times 10^5 \cdot 5 \times 10^{14} \cdot 10^{-9}) = 10^{-5}$ sec

$\tau_5^{\dagger}(\text{Cs}^+_{2}) = ([e] \cdot k_5)^{-1} = (10^9 \cdot 5 \times 10^{-9})^{-1} = 1$ sec

(1.1), (1.2), and (1.5) will not affect the change in ion and electron concentrations during and immediately after the flash because these reactions deplete charged particle concentrations in a characteristic time which is much longer than the pulse duration.

The orderings $\tau_{3a}^{\dagger}(\text{Cs}^+) \ll \tau_2^{\dagger}(\text{Cs}^+)$ and $\tau_{4a}^{\dagger}(\text{Cs}^+_{2}) \ll \tau_5^{\dagger}(\text{Cs}^+_{2})$ [note that these τ 's are calculated at equilibrium where, for any species s, $\tau_1^{\dagger}(s) = \tau_1^{\dagger}(s)$] indicate that reactions (1.3a) and (1.4a) will proceed to establish partial equilibrium concentrations of $\text{Cs}^+ \cdot \text{N}_2$ and Cs^+_{2} while the recombination reactions change the ion and electron concentrations relatively slowly.

This partial equilibrium is embodied in the relations

$$\frac{[\text{Cs}^+ \cdot \text{N}_2]}{[\text{Cs}^+][\text{N}_2]} = \frac{K_{3a}}{K_{-3a}}, \quad (1.9)$$

and

$$\frac{[\text{Cs}_2^+]}{[\text{Cs}][\text{Cs}^+]} = \frac{K_{4a}}{K_{-4a}} \cdot \frac{K_{3a}}{K_{-3a}} \quad (1.10)$$

Equilibrium relation (1.10) corresponds to the reaction $\text{Cs}_2^+ \rightleftharpoons \text{Cs} + \text{Cs}^+$ obtained by adding reactions (1.3a) and (1.4a). Once reactions (1.3a) and (1.4a) are shown to be fast enough to maintain partial equilibrium, the equilibrium relations need not correspond directly to the reaction channel. Relations (1.9) and (1.10) have been chosen to express the equilibrium condition in order to illustrate that the equilibrium concentrations of Cs_2^+ and $\text{Cs}^+ \cdot \text{N}_2$ are approximately decoupled.

Since N_2 and Cs are present in much larger quantities than Cs^+ , Cs_2^+ , or $\text{Cs}^+ \cdot \text{N}_2$ (as can be justified by the results of the calculation being described), the following major species relations can be written:

$$[\text{N}_2] = \text{constant} = 10^{19} \text{ cm}^{-3}, \quad (1.11)$$

and

$$[\text{Cs}] = \text{constant} = 4.5 \times 10^{14} \text{ cm}^{-3}. \quad (1.12)$$

From Equations (1.9) and (1.11) and Table 1.1 the ratio $[\text{Cs}^+ \cdot \text{N}_2]/[\text{Cs}^+] = [\text{N}_2] \cdot k_{3a}/k_{-3a}$ can be shown to be less than 1% at all temperatures greater than 500 K. Additionally, it has been shown that the recombination reactions are too slow to significantly affect charge concentration during the flash. Neglecting the $\text{Cs}^+ \cdot \text{N}_2$ concentration and the effects of recombination, charge conservation during the flash can be written

$$[\text{Cs}^+] + [\text{Cs}_2^+] = [+] \quad (1.13)$$

where $[+]$ denotes the concentration of positive (or negative) charge produced by the photoionization process. The charge produced by the flash is

$$[+] = [\text{Cs}] \cdot k_6 \cdot \Delta t = 4.5 \times 10^{14} \cdot 1 \cdot 10^{-3} = 4.5 \times 10^{11} \text{ cm}^{-3} \quad (1.14)$$

Equations (1.10), (1.12), (1.13), and (1.14) are sufficient to determine equilibrium concentrations of Cs_2^+ and Cs^+ ; the value for $[\text{Cs}^+]$ can then be used with Equations (1.9) and (1.11) to determine the $\text{Cs}^+ \cdot \text{N}_2$ concentration. The species concentrations obtained in this way are shown by

the curves plotted in Fig. 1.4, and compare well with the results of the numerical solution at $t=1$ ms which have been plotted as individual points over these curves. The results shown in Fig. 1.4 can be used to predict the relative rates of the recombination reactions which follow the flash.

Characteristic Times for Recombination

Shown in Fig. 1.5 are the characteristic reciprocal times $1/\tau$ for significant electron recombination by each of the processes (1.1), (1.2), and (1.5), at $t=1$ ms, immediately following termination of the flash. The quantity $1/\tau$ is a measure of the frequency of electron loss via a given recombination reaction. The continuous curves were calculated using the formulas shown in Table 1.2 evaluated for the concentrations given in Fig. 1.4. At temperatures above 1000 K reaction (1.2) is clearly the dominant loss mechanism immediately after the flash.

The numerical solutions shown in Figs. 1.1b, 1.2b, and 1.3b give detailed information about electron loss mechanisms for extended times after the flash. These plots correspond in temperature and time to Figs. 1.1a, 1.2a, and 1.3a. The frequency of electron loss by reaction i ,

$$\frac{1}{\tau_i^\downarrow (e)} = \frac{(\text{forward} - \text{backward reaction rate})}{[e]}$$

is shown for recombination reactions (1.1), (1.2), and (1.5) during plasma relaxation. The net reaction rate (forward - backward rate) must be considered for $t > 1$ ms when the reactions can approach equilibrium. At $t=1$ ms the net rate and forward rate are approximately equal. Generally the electron concentration and the net reaction rate change with time, hence this frequency is usually time dependent.

A recombination reaction is considered to be the dominant electron loss mechanism when its electron loss frequency exceeds the frequencies of all other competing loss mechanisms. If measurement of electron concentration decay is to be useful in determining the rate of reaction (1.2), experimental conditions must be chosen so that reaction (1.2) is the dominant electron loss mechanism. For all temperatures greater than

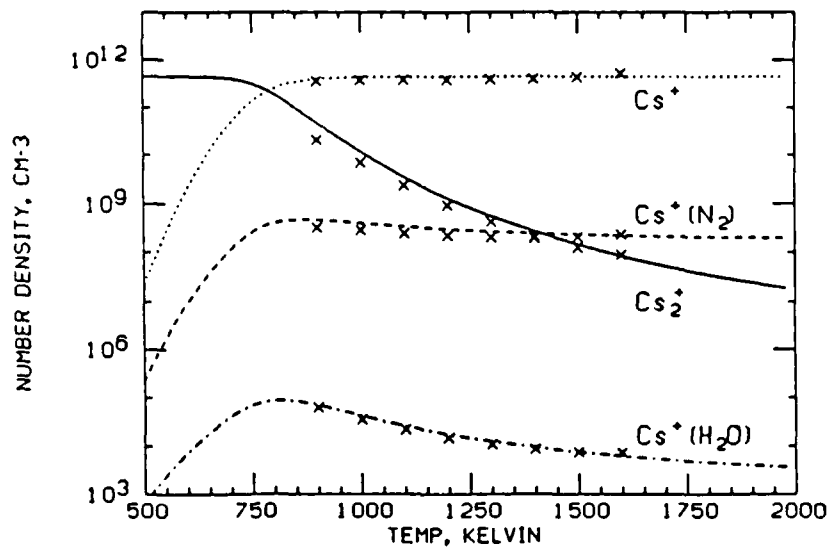


Fig. 1.4 Partial equilibrium species concentrations at $t=1$ ms (immediately after photoionization). Continuous lines correspond to analytical solution of equations (1.10)-(1.16); discrete points correspond to numerical solutions of kinetics equations as in Figs. 1.1-1.3.

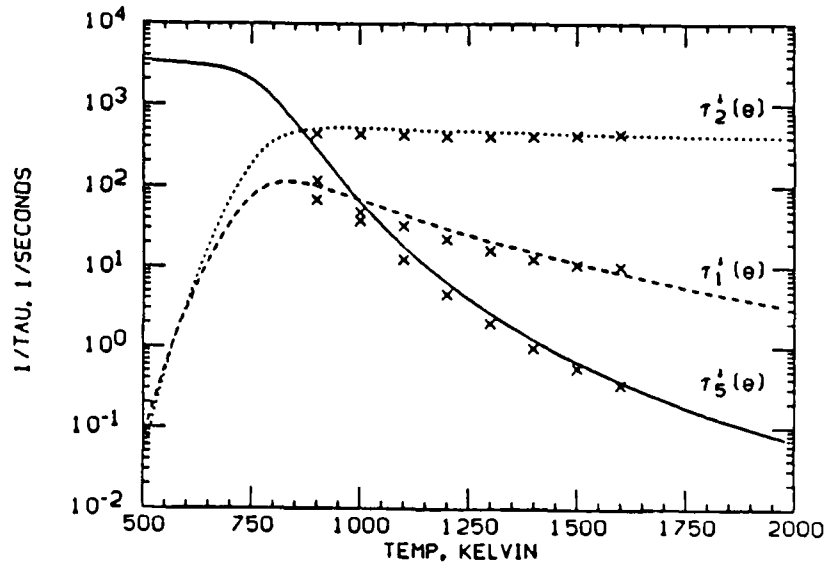


Fig. 1.5 Electron loss frequencies at $t=1$ ms (immediately after photoionization). Continuous lines correspond to the formulae of Table 1.2 and the concentrations of Fig. 1.4. Discrete points correspond to numerical solutions as in Figs. 1.1-1.3. For ambipolar diffusion, $1/\tau_{diff}^{\downarrow}(e) \lesssim 10 \text{ s}^{-1}$.

1000K, and all times shown, reaction (1.2) dominates reactions (1.1) and (1.5) in electron loss. The electron loss frequency due to ambipolar diffusion, $1/\tau_{diff}^{\downarrow}(e)$, (at about 1200 K and one atmosphere of N_2) is approximately constant at 10 sec^{-1} . As the electron concentration decays with time, $1/\tau_2^{\downarrow}(e)$, decreases because the reactions move toward an equilibrium balance where the forward and backward rates are equal. Electron concentration measurements are only useful while the resulting reduced electron loss frequency remains larger than $1/\tau_{diff}^{\downarrow}(e)$, hence for the conditions of Figs. 1.1-1.3 electron concentration measurements should be made in approximately the first 10 ms of recombination. Electron loss frequencies at one ms which are taken from numerical solutions similar to those shown in Figs. 1.1b, 1.2b, and 1.3b are plotted as discrete points with the analytical solution shown in Fig. 1.5. Both solutions agree that at temperatures above 1000 K, during the first ten milliseconds after photoionization, measurement of electron concentration decay will provide direct information about reaction (1.2).

Reaction 1.6 competes directly with reaction 1.2 for electrons, but the electron loss frequency can be expected to be low due to its dependence on the low concentration of $Cs^+ \cdot N_2$. Reactions 1.7 and 1.8 together constitute a channel for electron loss via recombination with Cs^+ . These three reactions have been included in an extended computer model of the kinetics. The results of the numerical calculation of concentrations and electron loss frequencies based on reactions (1.1) - (1.8) are shown in Figs. 1.6a and 1.6b (and can be compared with Fig. 1.2). Figure 1.6b indicates that reactions (1.6) and (1.7) are significant secondary electron loss mechanisms, but the primary electron loss mechanism remains reaction (1.2). Measurement of the rate of electron concentration decay will be a valid indication of the rate of reaction (1.2).

Impurities

The species Cs , Cs^+ , e , and N_2 are necessary for the experiment; other chemical species which may be formed from these cannot be avoided. In addition, the presence in the test cell of impurities due to

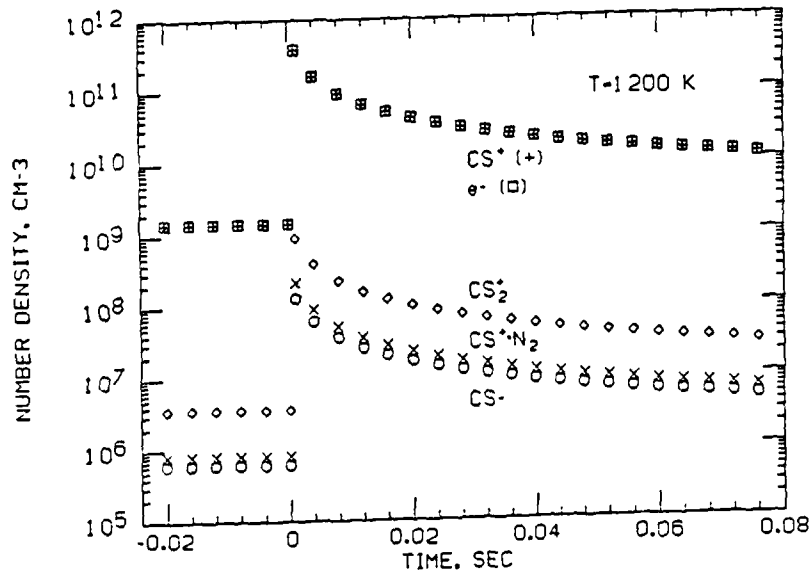


Fig. 1.6a Species concentrations from numerical solution of kinetics equations for reactions (1)-(8). $T=1200\text{K}$. The following initial species concentration remain roughly constant $[\text{Cs}]=4.5 \times 10^{14} \text{cm}^{-3}$; $[\text{N}_2]=10^{19} \text{cm}^{-3}$; $[\text{H}_2\text{O}]=10^{13} \text{cm}^{-3}$. Two distinct regimes are shown: $t < 0$, complete equilibrium; $t > 1 \text{ms}$, plasma relaxation. Photoionization occurs between these regimes.

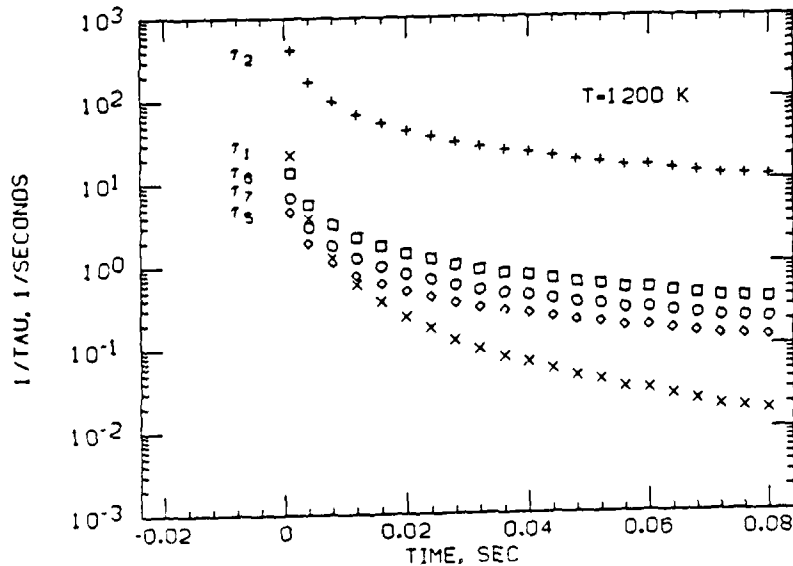


Fig. 1.6b Electron loss frequencies from numerical solution of kinetics equations for reactions (1)-(8). $T=1200\text{K}$. The following initial species concentrations remain roughly constant $[\text{Cs}]=4.5 \times 10^{14} \text{cm}^{-3}$; $[\text{N}_2]=10^{19}$; $[\text{H}_2\text{O}]=10^{13} \text{cm}^{-3}$. $1/\tau_i \equiv (d[e]/dt)_i/[e]$.

outgassing or impure reactant gases must be considered. Impurity concentrations can easily be kept small enough to ensure that N_2 is the dominant neutral partner in all reactions, but small amounts of radical species could substantially affect ion-molecule chemistry.

Water vapor is, of all impurities, most likely to be both sufficiently reactive and plentiful to have a significant effect. The amount of H_2O present in the N_2 charge will be minimized by passing the gas through a liquid nitrogen trap. The partial pressure of the H_2O will roughly correspond to the vapor pressure at 100 K, $P_v \sim 10^{-10}$ torr [1.4]. At 300 K this pressure corresponds to $[H_2O] = 5 \times 10^6 \text{ cm}^{-3}$. For a baked and pumped metal system a typical outgassing rate is 10^{-10} torr·liter/sec· cm^2 [1.5]. Assuming H_2O is a major constituent of the outgas and using design dimensions of the test cell with a period of about 30 hours between the end of pumping and the end of the experiment, $P_{H_2O} = 10^{-10} (\text{torr} \cdot \text{lit} / \text{sec} \cdot \text{cm}^2) \cdot 60 \text{ cm}^2 \cdot 10^5 \text{ sec} / 1 \text{ lit} = 6 \times 10^{-4}$ torr. At 300 K this pressure corresponds to $[H_2O] = 2 \times 10^{13} \text{ cm}^{-3}$. For one atmosphere of N_2 this H_2O concentration corresponds to an impurity level of one part per million. However, the water present will be very effectively scavenged by reducing reactions with Cs vapor. A reduction in H_2O concentration by a factor of 300 has been achieved by introducing Cs vapor into a 10^{-5} torr vacuum [1.6]. In light of scavenging $[H_2O] = 10^{13} \text{ cm}^{-3}$ appears to be a conservative worst case estimate.

Even assuming an amount of water vapor impurity equal to this worst case estimate, it can be shown that ion-molecule chemistry of water vapor in the plasma will not interfere with the primary experimental goal of measuring the rate of reaction (1.2). The association and switching reactions (1.3) and (1.4) can occur with N_2 replaced by H_2O ; related bond energies are $E_{Cs^+ \cdot N_2} = 6.7 \text{ kcal/mol}$ [1.7], and $E_{Cs^+ \cdot H_2O} = 13.7 \text{ kcal/mol}$ [1.8]. In relation to the measurement of the rate of reaction (1.2), reactions (1.3) and (1.4) provide a channel for the production of Cs_2^+ (which subsequently dissociatively recombines) and a loss mechanism for Cs^+ . It has been shown for the relatively fast reactions involving the $Cs^+ \cdot N_2$ cluster that a partial equilibrium calculation can be used to determine species concentrations before recombination begins. Partial

equilibrium represents a worst case since it allows the greatest advancement down the reaction channel which produces Cs_2^+ prior to the onset of recombination. Partial equilibrium may therefore be conservatively assumed for the reactions involving the $\text{Cs}^+\cdot\text{H}_2\text{O}$ cluster in a calculation which is analogous to the $\text{Cs}^+\cdot\text{N}_2$ partial equilibrium computation. Agreement between analytical and numerical solutions for $\text{Cs}^+\cdot\text{H}_2\text{O}$ concentration in Fig. 1.4 supports the validity of the partial equilibrium assumption. For equilibrium involving $\text{Cs}^+\cdot\text{H}_2\text{O}$ the governing equations are (1.10), (1.12), (1.13), (1.14),

$$\frac{[\text{Cs}^+\cdot\text{H}_2\text{O}]}{[\text{Cs}^+][\text{H}_2\text{O}]} = \frac{K_{3b}}{K_{-3b}} \quad (1.15)$$

and

$$[\text{H}_2\text{O}] = \text{constant} = 10^{13} \text{ cm}^{-3} \quad (1.16)$$

Equation (1.13) still accurately describes charge conservation since from equations (1.15) and (1.16) and Table 1.1, $[\text{Cs}^+\cdot\text{H}_2\text{O}] / [\text{Cs}^+] = [\text{H}_2\text{O}] \cdot k_{3b} / k_{-3b} < 0.01\%$ at all temperatures greater than 500 K. Both the $\text{Cs}^+\cdot\text{N}_2$ and $\text{Cs}^+\cdot\text{H}_2\text{O}$ clusters have been shown to occur in such small concentrations (relative to Cs^+) that the Cs_2^+ equilibrium concentration can be determined independently. In Fig. 1.4 the values for the Cs_2^+ and Cs^+ concentrations have been calculated first and then used to determine the $\text{Cs}^+\cdot\text{N}_2$ and $\text{Cs}^+\cdot\text{H}_2\text{O}$ concentrations. The $\text{Cs}^+\cdot\text{H}_2\text{O}$ cluster will not provide a significant loss mechanism for Cs^+ and the presence of water vapor will not affect the equilibrium concentration of Cs_2^+ calculated from Equations (1.10), (1.12), (1.13) and (1.14). Since the Cs_2^+ concentration is unchanged, previous statements about the negligible effect of dissociative recombination of Cs_2^+ still hold in the presence of water vapor impurities.

Conclusions

A model has been constructed to assess the role of several ion-molecule reactions [(1.3), (1.4), (1.5) and (1.6)] as well as two other reactions [(1.7) and (1.8)] which have not been addressed in previous analyses of the experiments being planned to measure the electron

recombination rate in plasmas under conditions of relatively low electron number density and high ambient pressure. The results of this study, based on numerical and analytical solutions of a full set of kinetic equations with rate coefficients estimated from information in the literature, indicate that for temperatures in the range of 1000 K to 1500 K, electron decay rate measurements during the first ten milliseconds of plasma relaxation can be identified with the three-body process $e + \text{Cs}^+ + \text{N}_2 \rightarrow \text{Cs} + \text{N}_2$, and can therefore be used to test theoretical predictions for this process. Our analysis of possible difficulties associated with the presence of a water vapor impurity indicates that in this temperature range the effect of the impurity is negligible.

It should be noted that considerable uncertainty exists for the values of many of the rate constants used in this study. However the study's conclusions are based on robust arguments about partial equilibria and the ordering of time constants which generally demonstrate that two reaction rates or two characteristic times differ by many orders of magnitude. The strength of the inequalities involved make these conclusions insensitive to reasonable uncertainties in rate constants.

Experimental Work

Description of Pulsed Photoionization Experiment

In the past year substantial progress has been made toward completing the construction of the facility for the pulsed photoionization experiment. The cesium cell with ancillary heating, temperature measurement, and vacuum systems has been completely fabricated. A breadboard circuit for the flashlamp has been built and preliminary pulse shapes have been obtained. This section describes the design of the experiment.

The radiation source chosen for photoionization is a pulsed short arc Xe lamp directed along the axis of a tube containing the test gas (e.g. Cs vapor and N_2). A schematic of the arrangement is shown in Fig. 1.7. The Cs vapor and N_2 are contained in a one inch diameter, twelve inch long inconel tube fitted with sapphire windows. The Cs pressure is one to ten torr and the nitrogen pressure is about one atmosphere. An

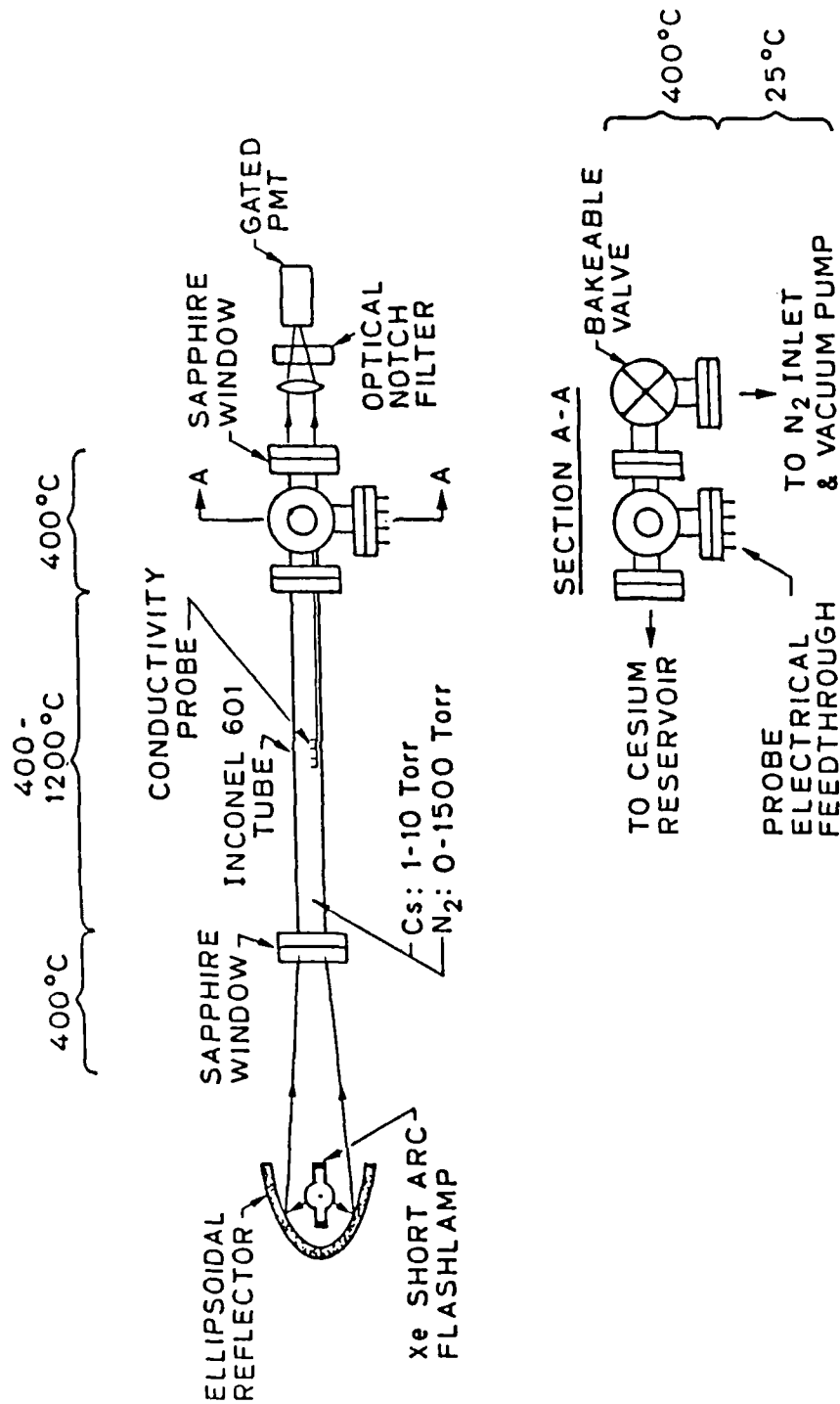


Fig. 1.7 Schematic of the apparatus for the pulsed photoionization experiment.

electric tube oven heats the Cs-N₂ mixture in the temperature range 400 to 1300 K. The sapphire window has 75% transmission of radiation down to 200 nm wavelengths so it is transparent to photons capable of singly ionizing ground state Cs atoms, i.e. $\lambda < 318$ nm, and opaque to photons capable of ionizing N₂, i.e. $\lambda < 200$ nm. The Xe flashlamp provides a 2 ms pulse of ionizing photons which is coupled to the Cs test cell by an ellipsoidal reflector.

A nonequilibrium, isothermal Cs plasma is produced by the radiation pulse. The free electrons are rapidly thermalized through collisions with the N₂. As the electrons begin to recombine with Cs⁺ in the presence of the nitrogen, the electron number density will be determined as a function of time. Methods for obtaining the electron density include measurements of the spectral emission from free-bound and high lying bound-bound transitions in Cs, as well as measurements of the electrical conductivity using a four pin conductivity probe. The time history of the electron number density is directly related to the rate coefficient for recombination on N₂.

The Cesium Cell

Inconel 601 (Huntington Alloys) was chosen as the Cs tube wall material because of its exceptional ability to resist oxidation and spalling at temperatures up to 1530 K. The 1 inch diameter tube will be heated at atmospheric pressure in a tube oven to temperatures in the range between 400 and 1300 K, and it must withstand oxidation by air externally, and reduction by Cs internally. Where the inconel tube extends beyond the oven, the temperature will be maintained at 700 K by two independent ovens. This end temperature is the maximum working temperature of the sapphire windows (necessary for transmitting ionizing and diagnostic radiation), instrumentation feed-through (for the conductivity probe), and vacuum flanges. Because this hardware cannot sustain the entire temperature range of the experiment, the cesium cell has end regions held at a lower temperature than the center region.

The Cs vapor pressure will be controlled by carefully monitoring the temperature of the Cs reservoir. The reservoir will be maintained 20 to

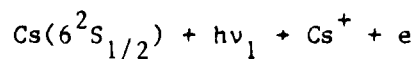
50 K cooler than any other part of the system to prevent Cs condensation in other parts of the system. The oxygen-free copper reservoir and the N₂ supply and vacuum pump are attached to the Cs cell by stainless steel tubing. The diffusion of the Cs vapor from the reservoir through the one inch diameter by 12 inch long tube to 90% of final concentration will occur in the time $t=0.47 x^2/D$ [1.24]. Here x is the tube length and $D=0.0911 (T/288)^{3/2}$ cm²/sec is the N₂-Cs binary diffusion coefficient. For $T=400$ K, $t=1.85$ hours. Although not unacceptably long, this mixing time will be decreased by natural convection. The option exists to spread the Cs throughout the reaction cell by flowing N₂ through the cell at a low flow rate relative to the rate of chemical reactions. The flowing system also has the advantage of constantly removing outgassed impurities from the reaction cell.

The N₂ number density will be determined from simultaneous temperature and pressure measurements before the cell is heated. To not exceed the 1% uncertainty estimated for the thermocouple measurement, a 1% limit on pressure measurement uncertainty is set. This accuracy must hold over the pressure range 200 to 1500 torr (resulting from a final pressure of 1500 torr with final temperatures ranging from 400 to 1300K.) These requirements will be met by a series of Wallace and Tiernan gages which span the desired pressure range.

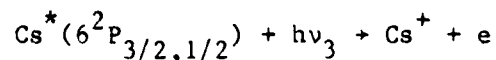
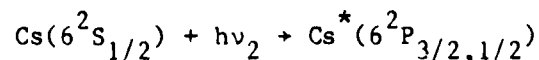
The tube and reservoir is attached via a bakeable valve to a liquid nitrogen trapped diffusion pump. Pressures of 10⁻⁶ torr are achievable with this system in order to remove impurities during initial bake out and subsequent gas changes.

Photoionization

Photoionization of the Cs by Xe flashlamp radiation occurs through both one and two photon processes. The single photon process converts a ground state 6s electron to a free electron as represented by the reaction



Here the photon energy, $h\nu_1$, must exceed the ionization potential of Cs, i.e. $\lambda < 318$ nm. Two-photon ionization first excites a ground state electron with a resonant photon; a second photon then ionizes the excited atom. The two steps are



The resonance wavelengths are $\lambda_2=852$ nm ($J=3/2$) or $\lambda_2=894$ nm ($J=1/2$), and ionization from the 6p state can occur with any photon of wavelength shorter than $\lambda_3 < 508$ nm ($J=3/2$) or $\lambda_3 < 494$ nm ($J=1/2$). The cross sections for ionization from the 6s and 6p levels are approximately 10^{-19} cm² and 10^{-17} cm² respectively. Contributions from the two photon process to total free electron production are estimated to be substantial [1.25].

The experimental arrangement is greatly simplified by positioning the light source away from the Cs cell and the heat of the reaction zone. Placing the source outside the cell necessitates directing the light through a sapphire window at the end of the inconel tube. To produce a collimated, intense photon flux, a high radiance lamp is required. We have chosen a five atmosphere Xenon short arc lamp, (L-2369, manufactured by ILC Technology of Sunnyvale, CA.) This lamp has a seven mm arc length and a synthetic fused silica envelope. It is designed for pulsed operation at a maximum energy input of 300 Joules per pulse. Pulsed operation [1.26, 1.27] and the synthetic fused silica envelope enhance ultraviolet output from the lamp. The short arc lamp will be aligned along the axis of an ellipsoidal, aluminum reflector. (The A-5000, 1000 watt reflector is sold by Photon Technology inc., Princeton, N.J.). The arc is imaged at the far focus with $f/2.5$ optics by positioning the arc at the near focus of the ellipsoid. The resulting beam diverges with a half angle of 11 degrees, and it can be aimed directly through the sapphire window into the tube. Grazing incidence and high reflectivity of the polished metal tube interior surface will insure a uniform photon flux through the cell's length.

A multiple mesh pulse forming network has been prototyped; it provides a roughly rectangular current pulse to the arc lamp. Pulse width is 3 ms, and pulse height will be 2,000 amps. To insure negligible interference by photoionization during the measured plasma decay, the current pulse falls from its maximum value to zero in 0.9 ms.

Diagnostics

A four pin plasma conductivity probe, developed at Stanford in connection with research on MHD plasmas, appears to be well suited for the work proposed here. The principle of operation of the probe is to measure the current I that flows when an ac voltage is applied between the outer pair of pins (i.e. electrodes) of a linear array of four pins, and to measure simultaneously the resulting potential difference δV between the inner pair of pins. Since J (current density) is proportional to I and δV is proportional to E (electric field), it follows from Ohm's Law, $E = J/\sigma$, that $\delta V = K I/\sigma$ and therefore that $\sigma = K dI/d(\delta V)$. Here σ denotes the electrical conductivity and K is a calibration constant that depends only on the geometric features of the probe. (In practice, $\delta V = K I/\sigma + \text{constant}$, but this constant plays no role upon differentiation.) The constant K can be determined by immersing the probe in a liquid electrolyte (e.g. aqueous KCl) solution.

The conductivity is then related to the electron number density by the relation $\sigma = (n_e e^2)/(m_e \nu_{eh})$, where ν_{eh} is the electron-heavy collision frequency and e is the electronic charge. Temporal resolution of 50 μ s, corresponding to operation at 20 kHz has been demonstrated [1.28]. Initially this probe will be tested on a steady state thermal plasma. An equilibrium electron concentration of $3.6 \times 10^{10} \text{ cm}^{-3}$ can be achieved by heating the Cs cell to 1300 K and the Cs reservoir to 630 K corresponding to a vapor pressure of 5 torr. The four pin probe measurement will be compared to equilibrium calculations of electron concentration based on Cs reservoir and cell temperature measurements. The probe will also be compared to optical diagnostic measurements.

Measurements of the recombination radiation continuum have been used to measure electron densities as low as $3 \times 10^{13} \text{ cm}^{-3}$ in the afterglow of

a Cs-Ar discharge [1.29, 1.30]. In this work [1.29, 1.30] a monochromator was used for spectral filtering. By employing a 50 Å filter in place of the monochromator, calculations indicate it should be possible to increase the collected radiation by a factor of the order of 10^3 and therefore to lower the limit of measureable, transient n_e to about 10^{12} cm^{-3} . This limit can be lowered still further to 10^{10} cm^{-3} when measurements are made on a steady state plasma. Hence optical emission diagnostics should provide a check for the conductivity probe during testing on the thermal plasma. Upon successful testing in a steady state plasma, the conductivity probe will be used to measure electron densities in the plasma afterglow.

At present, a simulated probe and high impedance amplifier have been built and tested with a 1 MΩ simulated plasma resistance. Successful performance has been obtained at frequencies up to 500 Hz. Higher frequency operation is hampered by capacitive coupling between probe leads. The problem of stray capacitance is currently being considered.

Summary

A detailed analytical and numerical model has been constructed and used to gain understanding of reaction kinetics in the pulsed photoionization experiment. The model has demonstrated the feasibility of determining the three-body recombination rate of the reaction $e + \text{Cs}^+ + \text{N}_2 + \text{Cs} + \text{N}_2$ through measurement of the rate of electron concentration decay, provided experiments are performed at temperatures of approximately 1000K or greater. Much of the experimental apparatus has been constructed. The reaction cell and ancillary heating and vacuum systems have been completed, and extensive development has been done on the pulsed flashlamp system.

2.2 Discharge Effects: Plasma-Electrode Interaction

Introduction

The structure of the plasma-sheath electrical boundary layer between an electrode and a weakly ionized thermal plasma, and the mechanisms of current transfer are subjects of considerable importance for a number of plasma devices and applications. These include arc discharges, thermionic converters, MHD generators and MPD thrusters. Important practical aspects of the interaction of electrodes with a plasma concern the voltage drop between the plasma and the electrode, and the conditions determining the transition from diffuse to constricted modes of current transfer. Operation of both cathodes and anodes in a constricted mode leads to electrode erosion which sets a practical limit to electrode life.

While it has been the subject of considerable research over many decades, the plasma-electrode boundary layer is still poorly understood [2.1,2.2]. The difficulty in analyzing this region stems from the inherent nonlinearities which result from the interaction of electrical, thermal, fluid dynamic and electrode surface effects.

This work is directed towards providing a more complete understanding of the plasma-electrode interaction for the case of flowing, seeded, thermal plasmas at pressures of the order of one atmosphere, and involves both theoretical and experimental components.

Consider a channel flow of thermal plasma which might be either a noble gas or combustion products gas seeded to a suitable level (~ 1%) with cesium or potassium. We may define the electric boundary layer as that region near the channel walls, composed of high temperature insulators and electrodes, where charged particle nonequilibrium effects become significant and even dominant. Normally, the walls have to be operated at temperatures less than that of the core flow plasma because of material limitations.

On physical and dimensional grounds the region between the core plasma and the electrode surface can be divided into a number of overlapping layers of decreasing scale. Proceeding from the core plasma to the electrode these layers may be listed as follows (see Fig. 2.1):

- (i) The gasdynamic boundary layer of scale $\delta \sim 10^{-2}m$, depending on distance along the channel, and comprising both a velocity and thermal boundary layer. In this region the plasma is in thermodynamic equilibrium at the local temperature $T(x)$ and supports an electric field $E(x) = J/\sigma(x)$ where J is the current

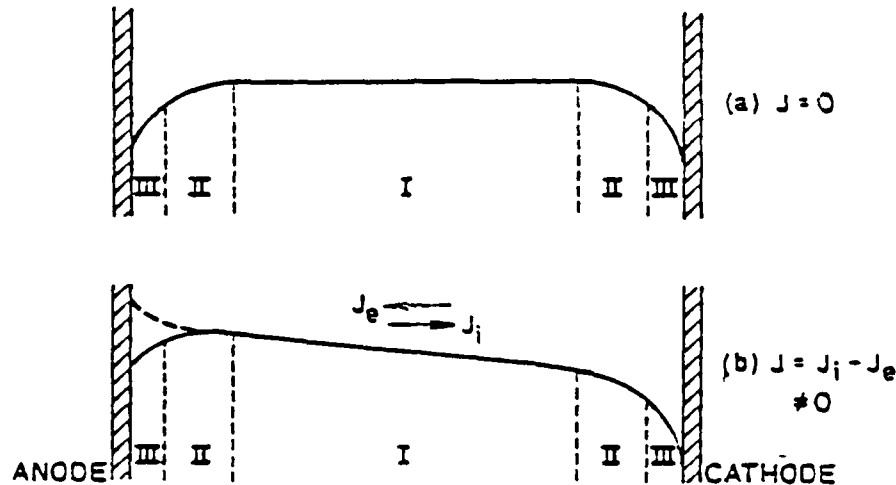


Figure 2.1 Potential distribution across plasma diode.

- I Equilibrium Plasma
- II Ionization Non-Equilibrium Layer
- III Sheath. (Not to scale)

density and $\sigma(T)$ is the equilibrium electrical conductivity.

- (ii) The ionization nonequilibrium (or ambipolar diffusion) layer of scale $T_R \equiv (2D_a/\beta n_\infty^2)^{1/2} \sim 10^{-3}m$. Here $\beta(T) \sim 10^{-20} T^{-9/2} m^6/sec$ is the three-body recombination coefficient divided by the plasma concentration at infinity, n_∞ , and D_a is the ambipolar diffusion coefficient. In this layer the generation rate of electron-ion pairs exceeds the recombination rate to supply net fluxes of charged particles. In the absence of current ($J=0$) the equal electron and ion fluxes flow to the electrode where they recombine. When $J \neq 0$, and in the absence of electrode emission, these fluxes flow towards or away from the electrode and constitute the only source of net current. A potential drop of scale (kT/e) develops such that the walls are normally negative relative to the plasma, except for an anode at large currents when the potential fall becomes positive (see broken line in Fig. 2.1). The self-

consistent field adjusts the charged particle fluxes to match the core current to that entering the sheath overlying the electrode. In this layer quasi-neutrality $n_e \approx n_i$ exists.

(iii) The sheath of scale equal to the Debye length $\lambda_D \equiv (\epsilon_0 kT/n_e e^2)^{1/2}$, typically 10^{-6} m. In this layer charge neutrality is not preserved and large electric fields develop which must be calculated from Poisson's equation. The sheath serves to match the charged particle fluxes from the ambipolar diffusion layer to the absorption and emission processes for charged particles at the electrode surface. For a cathode, the sheath structure and potential drop is critically dependent on the electron emission process and thus depends on the temperature and surface state which control the work function. With electron emission, a double sheath forms at a cathode, and consists of an electron rich sheath next to the electrode and the usual positive ion sheath between the electron sheath and the neutral plasma. For an anode that does not emit ions, the current transfer is effected purely by the collection of electrons from the plasma. The situation is different in those cases (e.g., in thermionic converters) where the anode can emit ions.

(iv) The Knudsen layer where free molecule flow takes over from a continuum (fluid) description and the appropriate scale is the mean free path. The mean free paths for electrons and ions are of order $\lambda_e \sim \lambda_i \sim 10^{-6}$ m and are thus comparable to λ_D . Our calculations show that the sheath is typically many Debye lengths thick, so that the sheath is, for the most part, collision dominated.

It should be emphasized that the four layers distinguished above are overlapping and no sharp boundaries can be distinguished. Moreover, the scale lengths are nominal ones based on core values rather than local conditions. In general the scale lengths are ordered according to $\delta \gg \lambda_R \gg \lambda_D \sim \lambda_e \sim \lambda_i$.

As the current density J is increased from zero, the potential drop at the cathode increases and more ions than electrons are collected. However this condition only holds for very small currents ($\lesssim 1$ mA/cm²), at which point the collected electron flux becomes zero and the current at the cathode is carried entirely by arriving ions. For higher

currents, of technical interest, the cathode must emit electrons. Of the known emission processes, only thermionic emission (including field-assisted, Schottky emission) is relevant. Depending on conditions, particularly the cathode material, temperature and work function, diffuse emission persists up to some current density when there is a transition to a constricted discharge terminating in one or more arc cathode spots.

At the anode it might be expected that large currents up to $J \sim en_e \bar{c}_e / 4$, the random electron current ($\sim 250 \text{ A/cm}^2$), could be collected as a result of the reducing sheath potential drop. However it is commonly observed that constrictions in the form of anode glow spots occur at much lower currents and that the sheath potential drop changes sign as indicated in Fig. 2.1. The reason for this behavior is hitherto unexplained, but it is generally thought to be related to the creation of a highly conducting discharge channel which penetrates the lower conductivity boundary layer plasma.

From the foregoing discussion it is clear that the physical processes involved are extremely complex and that experimental data are vital to guide the theoretical modeling.

Research Objectives

1. To observe and record the current-voltage characteristics and the transition from diffuse to constricted discharge modes for electrodes immersed in a flowing, atmospheric pressure thermal plasma.
2. By analytical and computer modeling, to predict the current-voltage characteristics for anodes and cathodes under diffuse conditions and to compare these predictions with the experimental results.
3. To use the insight provided from objectives 1 and 2 above to more fully understand the constriction process.

Status of Research

To date, we have concentrated our efforts on the theoretical aspects of the research objectives.

Theoretical Work

The approach adopted for theoretical modeling is to start off with the simplest relevant model and to introduce the complexities of the complete problem one at a time. To this end, the plasma-sheath problem for a plane electrode in contact with a uniform, equilibrium, weakly-ionized plasma has been formulated in some generality. By assuming that the plasma is isothermal and stationary, the complexities associated with the gasdynamic thermal boundary layer and Joule heating are, for the present, eliminated to allow the essential plasma physics aspects of the problem to be studied.

This formulation in terms of the conservation equations for the electron and ion concentrations and momenta (including inertia), together with Poisson's equation, gives a uniform description of the ionization nonequilibrium layer and sheath, in both the collisionless and collision dominated regimes, without having to resort to an arbitrary division and matching of the separate regions.

To the present time, under this grant, this plasma-sheath problem has been investigated in the continuum (collision-dominated) limit, neglecting the inertia terms, which is applicable to MHD and similar high pressure plasma. In this case the governing equations are:

$$\frac{d\bar{\Gamma}_e}{d\bar{x}} = \bar{n} = (1 - \bar{n}_e \bar{n}_i) \bar{n}_e \quad (2.1)$$

$$\frac{d\bar{\Gamma}_i}{d\bar{x}} = \bar{n} = (1 - \bar{n}_e \bar{n}_i) \bar{n}_e \quad (2.2)$$

$$\frac{d\bar{n}_e}{d\bar{x}} = -\bar{n}_e \bar{E} - \frac{4\nu}{(1+\nu)} \bar{\Gamma}_e \quad (2.3)$$

$$\frac{d\bar{n}_i}{d\bar{x}} = \bar{n}_i \bar{E} - \frac{4}{(1+\mu)} \bar{\Gamma}_i \quad (2.4)$$

$$\frac{d\bar{E}}{d\bar{x}} = \frac{1}{\epsilon^2} (\bar{n}_i - \bar{n}_e) \quad (2.5)$$

together with the subsidiary relations

$$\bar{J} = \frac{4\mu}{(1+\mu)^2} (\bar{\Gamma}_i - \bar{\Gamma}_e) \quad (2.6)$$

$$\bar{\phi} = - \int_0^{\bar{x}} \bar{E} d\bar{x} \quad (2.7)$$

Here x is normalized on the ion recombination distance $\ell_R \equiv (2D_a/\beta n_\infty^2)^{1/2}$ where D_a is the ambipolar diffusion coefficient and β is the three-body recombination coefficient. The electron and ion concentrations are normalized on n_∞ while the net generation rate \dot{n} is normalized on βn_∞^3 . The potential ϕ is normalized on (kT/e) while the electric field is normalized on $E_R \equiv (kT/e\ell_R)$. The fluxes are normalized on $\Gamma_R \equiv (2D_a n_\infty/\ell_R)$ and the current density is normalized on $J_R \equiv en_\infty (\mu_e + \mu_i)$ $E_R \equiv \sigma_\infty E_R$ where σ_∞ is the electrical conductivity for $x \rightarrow \infty$.

There are three parameters to be specified: the mobility ratio $\mu \equiv (\mu_i/\mu_e) \ll 1$, a function only of the type of ion and background gas; $\epsilon \equiv (\lambda_D/\ell_R) \ll 1$, the ratio of the Debye length to the ion recombination length; and \bar{J} , the normalized current density.

For a perfectly absorbing (catalytic), non-emitting electrode, the boundary conditions at $\bar{x}=0$ are the familiar continuum ones:

$$\bar{n}_e(0) = \bar{n}_i(0) = 0 \quad (2.8)$$

For an electrode which emits electrons (or ions) the continuum boundary condition is that $\bar{n}_e(0)$ (or $\bar{n}_i(0)$) has a prescribed non-zero value. However, it is necessary to relate the value of $\bar{n}_e(0)$ (or $\bar{n}_i(0)$) to the actual value of the emission flux density from the surface. By considering the evolution of the charged particle distribution function across the Knudsen layer, the following relation has been derived

relating the electron saturation emissive flux $J_e^+(0)$ at the surface and the values of $\bar{n}_e(0)$ and $\bar{\Gamma}_e(0)$ in the continuum description.

$$J_e^+(0) = - \frac{2\mu}{(1 + \mu)^2} [\bar{n}_e(0) (\bar{c}_e/2v_R) + \bar{\Gamma}_e(0)] \quad (2.9)$$

where $v_R \equiv (2D_a/l_R)$ is a reference diffusion velocity and $\bar{c}_e \equiv (8kT/\pi m_e)^{1/2}$ is the electron mean thermal speed.

Physically, $J_e^+(0)$ is the electron emission saturation current density given by the Richardson-Dushman law

$$J_e^+(0) = - AT^2 \exp - (\phi_w/kT) \quad (2.10)$$

where ϕ_w is the surface work function and $A \approx 1.2 \times 10^6 \text{ A/m}^2 \text{K}^2$. Equation (2.10) is applicable when the electric field at the electrode is zero or decelerating for emitted electrons ($E(0) > 0$). When there is an accelerating field at the electrode ($E(0) < 0$), field-enhanced emission due to the Schottky effect is applicable:

$$J_e^+(0) = - AT^2 \exp - [\phi_w - (-e^3 E(0)/4\pi\epsilon_0)^{1/2}]/kT \quad (2.11)$$

$$\approx J_{e0}^+ \exp (0.44 (-E(0))^{1/2}/T) \quad (2.11b)$$

where J_{e0}^+ is the emission given by Eq. (2.10). In practice very large accelerating fields are required to cause significant enhancement of the emission.

The case of ion emission at the electrode likewise corresponds in general to the boundary condition $\bar{n}_i(0) > 0$. However, ion emission only occurs for the relatively rare combination of a gas whose ionization energy is comparable with or less than the work function of the (bare) surface, e.g., the heavier alkali metal vapors combined with refractory metals, such as are employed in thermionic converters. Depending on the electrode temperature, the surface is more or less covered with a layer of the alkali metal, which lowers the work function and generally promotes electron emission as well as ion emission. For most plasma

devices, including MHD and MPD applications, the possibility of significant ion emission is negligible.

The remaining boundary conditions for the equation set (2.1)-(2.5) are taken as that the values of $\bar{\Gamma}_e$, $\bar{\Gamma}_i$ and \bar{E} at $x \rightarrow \infty$ should match those given by the quasi-neutral approximation [2.3] which will now be briefly summarized.

In the quasi-neutral solution we put $\bar{n}_e = \bar{n}_i = \bar{n}$ and discard Poisson's equation. With the boundary conditions $\bar{n}(0) = 0$, $\bar{n}(\infty) = 1$, we obtain the analytical results

$$\bar{n} = \tanh \bar{x} \quad (2.12)$$

$$\dot{\bar{n}} = \text{sech}^2 \bar{x} \tanh \bar{x} \quad (2.13)$$

$$\bar{\Gamma}_e = -\frac{1}{2} \text{sech}^2 \bar{x} - \frac{(1+\mu)}{4\mu} \bar{J} \quad (2.14)$$

$$\bar{\Gamma}_i = -\frac{1}{2} \text{sech}^2 \bar{x} + \frac{(1+\mu)}{4} \bar{J} \quad (2.15)$$

$$\bar{E} = \left[-\left(\frac{1-\mu}{1+\mu}\right) \text{sech}^2 \bar{x} + \bar{J} \right] \coth \bar{x} \quad (2.16)$$

$$\bar{\phi} = \ln \tanh \bar{x} - \bar{J} \ln \sinh \bar{x} \quad (2.17)$$

It is noteworthy \bar{n} and $\dot{\bar{n}}$ are independent of \bar{J} , and that \bar{E} has a simple pole while $\bar{\phi}$ has a logarithmic pole at $\bar{x} = 0$. The profiles of \bar{n} and $\dot{\bar{n}}$ are shown in Fig. 2.2a, while the potential profiles for various \bar{J} are shown in Fig. 2.2b.

Within the past year, a numerical code for solution of the full equations has been perfected. This uses the method of quasilinearization and orthonormalization of the governing equations. A large number of numerical solutions have been obtained over wide ranges of the parameter values μ , ϵ and \bar{J} with different levels of electron and ion emission, corresponding to different values of the boundary conditions $\bar{n}_e(0)$, $\bar{n}_i(0)$. Our aim is to provide a comprehensive physical understanding of the nature of the various forms of solution and to document

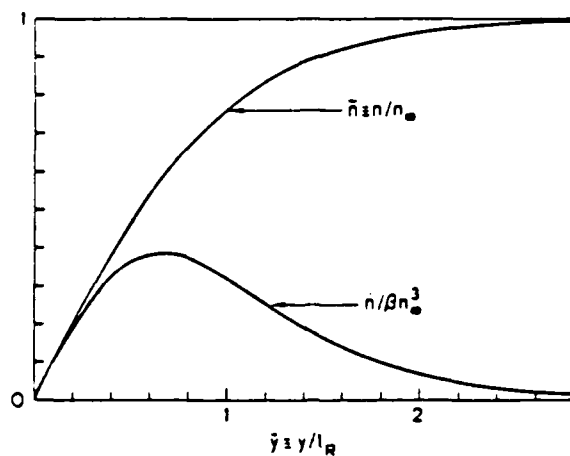


Figure 2.2a. Profiles of normalized charged particle concentrations and net generation rate.

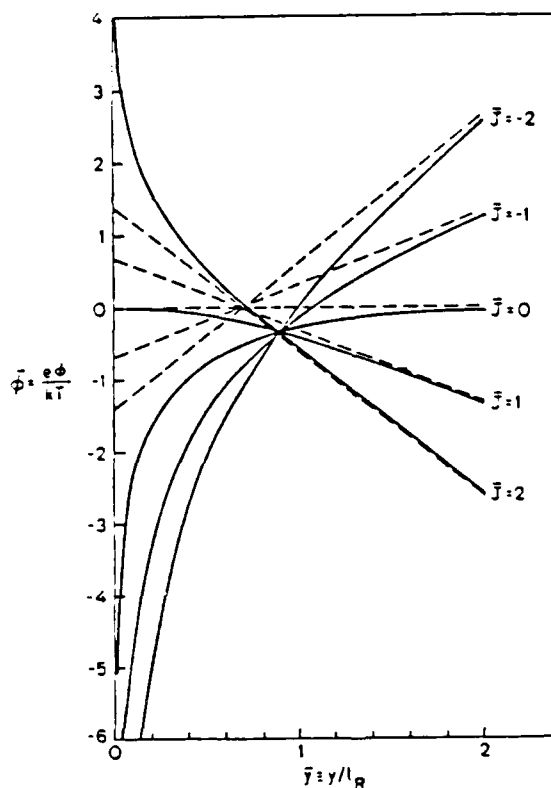


Figure 2.2b. Profiles of the normalized potential as a function of normalized current density: $\bar{J} < 0$, cathode; $\bar{J} > 0$, anode. Broken lines indicate the asymptotes corresponding to the uniform electric field in the distant plasma for the quasi-neutral approximation.

the dependence of various important quantities such as the sheath thickness and potential drop as a function of the parameters.

The results have been organized into three basic cases: (i) an electrically isolated (floating) electrode ($J=0$) without and with electron emission, (ii) a cathode ($J<0$) without and with electron emission and (iii) an anode ($J>0$) without and with both ion and electron emission. The first case, which has been completed and written up [2.4] is relevant to the electrodes of MHD generators at open circuit and is also related to the theory of thermionically emitting probes, first introduced by Langmuir. The second and third cases, for which reports are currently being written, are relevant respectively to the cathodes of a variety of high pressure plasma devices and to the emitters of thermionic converters in the ignited mode as well as to the anodes of seeded, noble gas MHD and MPD devices. A few of the important results for case (i) may be illustrated, as follows.

For $J=0$ and zero electron emission ($n_e(0) = 0$), the profiles of \bar{n}_e , \bar{n}_i , \bar{n} , and \bar{E} and $\bar{\phi}$ are illustrated in Figs. 2.3 and 2.4, for the cases of $\nu = 1/300$ (typical of combustion MHD plasmas) and $\epsilon = 10^{-1}, 10^{-2}$. In Fig. 2.3a, for $\epsilon = 10^{-1}$, it is seen that both \bar{n}_e and \bar{n}_i lie well below the value \bar{n}_{QN} given by the quasi-neutral approximation, with $\bar{n}_i > \bar{n}_e$, corresponding to a positive ion sheath. As a result the position of maximum net generation \bar{n} occurs further from the electrode ($\bar{x} = 1.125$) than that of the quasi-neutral solution ($\bar{x} = 0.658$). If we define the sheath strength as

$$\Delta \equiv |n_i - n_e| / (n_i + n_e)/2 \quad (2.18)$$

and (arbitrarily) define the plasma-sheath boundary as corresponding to $\Delta = 0.1$, then the boundary occurs at $\bar{x} = 0.815$, corresponding to a sheath thickness of $8.15 \lambda_D$. As ϵ is decreased (Fig. 2.4a) the sheath is thinner on the \bar{x} scale, but on the Debye length scale it increases to $17.14 \lambda_D$. Also, as ϵ is decreased, the position of maximum generation tends to that given by the quasi-neutral solution. The sheath thickness and position of maximum generation are given as a function of

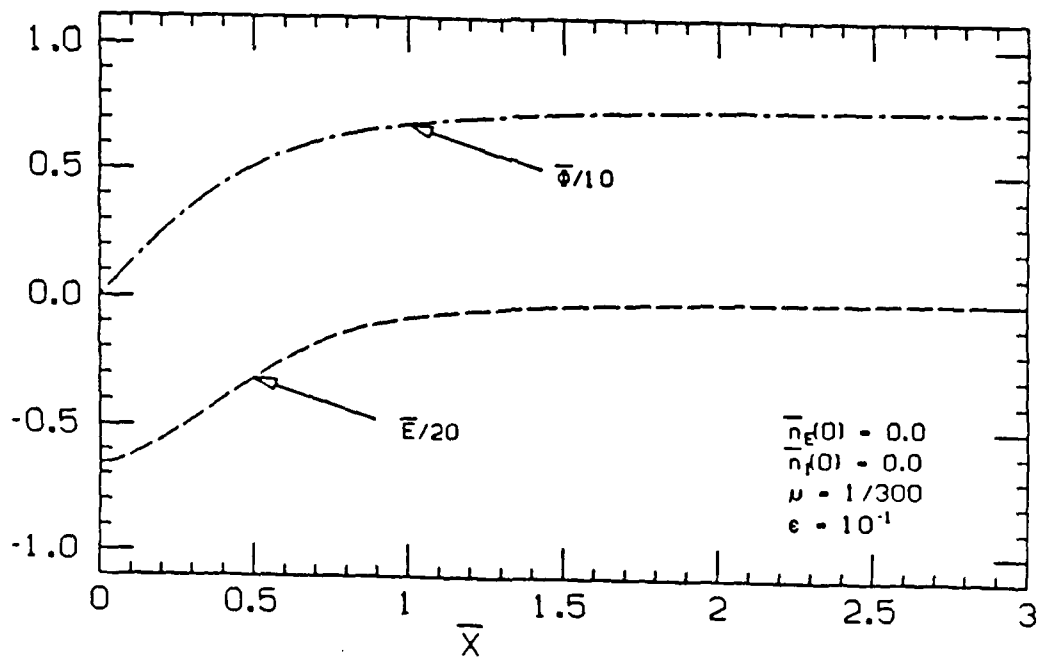
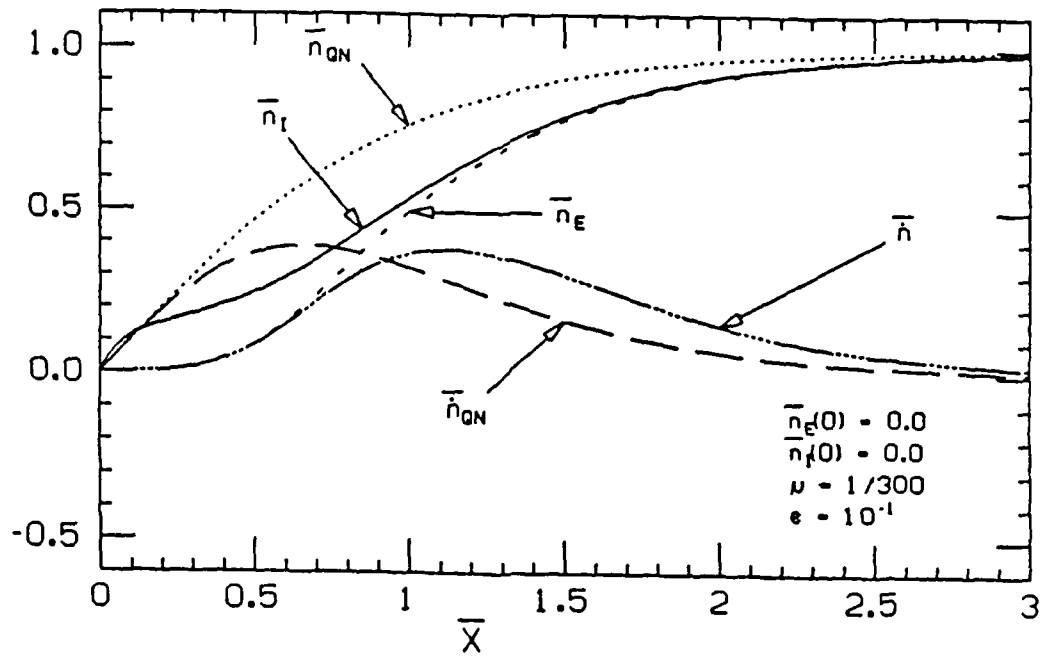


Figure 2.3 Profiles of: a) \bar{n}_e , \bar{n}_i , \bar{h} compared with those of quasi-neutral approximation, \bar{n}_{QN} , \bar{n}_{QN} ; b) \bar{E} and $\bar{\Phi}$; parameter values $\nu = 1/300$, $\epsilon = 10^{-1}$, $\bar{J} = 0$, $\bar{n}_e(0) = \bar{n}_i(0) = 0$.

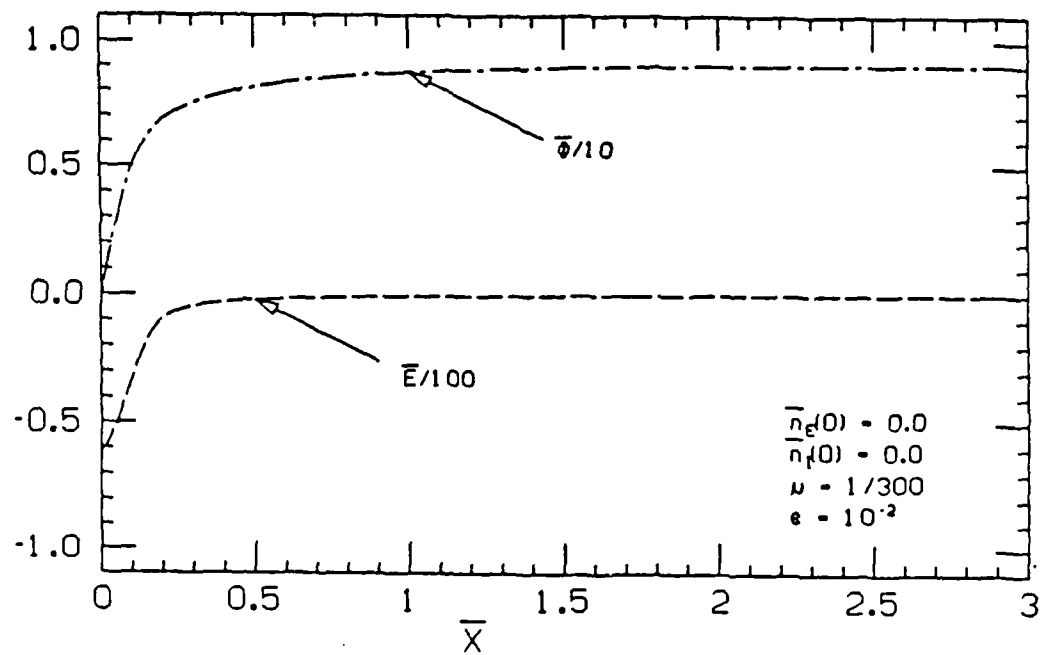
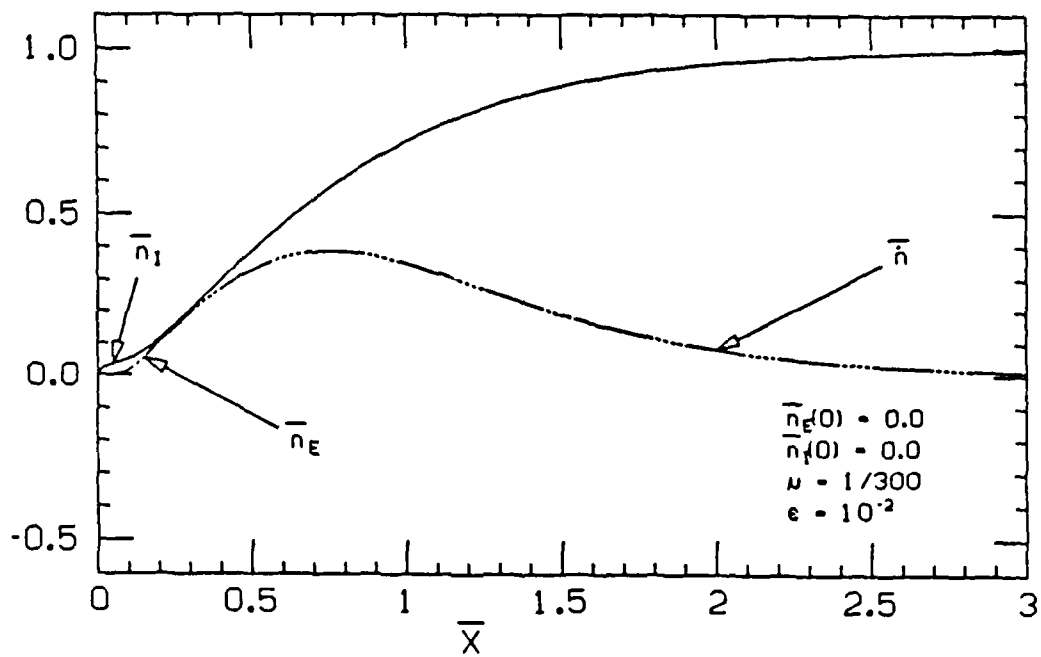


Figure 2.4. Profiles of: a) \bar{n}_e , \bar{n}_i , \bar{n} ; b) \bar{E} and $\bar{\Phi}$; parameter values $\nu = 1/300$, $\epsilon = 10^{-2}$, $\bar{J} = 0$, $\bar{n}_e(0) = \bar{n}_i(0) = 0$.

ϵ (10^{-1} - 10^{-3}) in Table 2.1. It may be noted that for typical combustion MHD conditions ($\epsilon = 10^{-3}$) the sheath is 36.3 Debye lengths thick. Since, for the same conditions, the electron and ion mean free paths are comparable to the Debye length ($\sim 10^{-6}$ m), this justifies the assumption of a collision-dominated sheath inherent to the continuum analysis. The profiles of \bar{E} and $\bar{\phi}$ in Figs. 2.3b and 2.4b show that \bar{E} increases strongly and $\bar{\phi}$ increases moderately as ϵ decreases. The values of the surface field $\bar{E}(0)$, and the total potential drop $\Delta\bar{\phi}_{\text{total}}$, are given in Table 2.1 as a function of ϵ . Another interesting result is that $\bar{\Gamma}_e(0) = \bar{\Gamma}_i(0)$, which equals the integral of the net generation rate \dot{n} , remains fixed at the value of $-1/2$ given by the quasi-neutral solution, despite the change in the profile of \dot{n} in the presence of the sheath.

Table 2.1 Non-emitting Electrode ($J = 0$) : Ion Sheath Thickness (in Debye lengths), Position of Maximum Generation Rate, Surface Field, and Total Potential Drop vs ϵ for $\mu = 1/300$.

ϵ	$\Delta x_{is}/\lambda_D$	Position of \dot{n}_{max}	$\bar{E}(0)$	$\Delta\bar{\phi}_{\text{total}}/(kT/e)$
10^{-1}	8.51	1.13	-13.2	-7.53
$10^{-3/2}$	11.73	0.86	-28.5	-8.30
10^{-2}	17.14	0.76	-61.3	-9.06
$10^{-5/2}$	25.20	0.69	-132.1	-9.83
10^{-3}	36.30	0.68	-284.5	-10.61

The profiles of \bar{n}_e , \bar{n}_i , \dot{n} , and of \bar{E} and $\bar{\phi}$ for $\mu = 1/300$ and $\epsilon = 10^{-1}$ with increasing values of electron emission, $\bar{n}_e(0) = 0.1, 0.5$ and 1.0 are shown in Figs. 2.5 through 2.7. The presence of electron emission introduces an electron-rich sheath adjacent to the electrode, followed by the usual ion sheath. With increasing electron emission, the width and strength of the electron sheath increases while the strength and

width of the ion sheath decreases. As a result, the total potential drop decreases dramatically; the electrode potential floats up towards the plasma potential, becoming equal to it for $\bar{n}_e(0) = 1$. This behavior is consistent with the use by Langmuir and others of a thermionically emitting probe to measure the plasma potential. For a given value of ϵ , there is a critical value of electron emission, measured by $\bar{n}_e(0)_{crit}$, equal to 0.223 for $\epsilon = 10^{-1}$, at which the surface field changes sign from negative to positive and a potential minimum occurs at the electrode surface. As $\bar{n}_e(0)$ is increased above the critical value, the potential minimum moves out from the electrode surface and the depth of the potential well increases, as is clear from Figs. 2.6b and 2.7b. There is also a minimum in \bar{n}_e associated with the potential minimum, due to the fact that the electrons approximately satisfy the Boltzmann relation $\bar{n} \propto \exp \bar{\phi}$. It should also be noted that although the electrode potential floats up to the plasma potential for $\bar{n}_e(0) = 1$, the plasma-sheath region is not, by any means, a region of uniform potential and charged particle concentration.

To our knowledge, this work represents the first satisfactory quantitative analysis of an emitting, floating electrode, and shows significant differences from the very approximate treatment originally given by Langmuir. Figure 2.8 shows the total potential drop as a function of electron emission ($\bar{n}_e(0)$) for various values of ϵ . It indicates that except for very small values of emission, the potential drop is independent of ϵ , and that while the electrode potential approaches the plasma potential for relatively small values of $\bar{n}_e(0)$, it only tends to exact equality as $\bar{n}_e(0)$ tends to unity.

One other, unexpected, result should be mentioned. With increasing electron emission, there is a significant shift of the region of net generation to the electrode surface, because of the enhanced value of \bar{n}_e in the electron sheath. However, despite the dramatic change in the profile of \bar{n} , the integral of the net generation rate (for $\bar{J}=0$) i.e. $\bar{\Gamma}_t(0) = - \int \dot{\bar{n}} d\bar{x}$, remains essentially invariant at the value $- 1/2$ given by the⁰ quasi-neutral approximation.

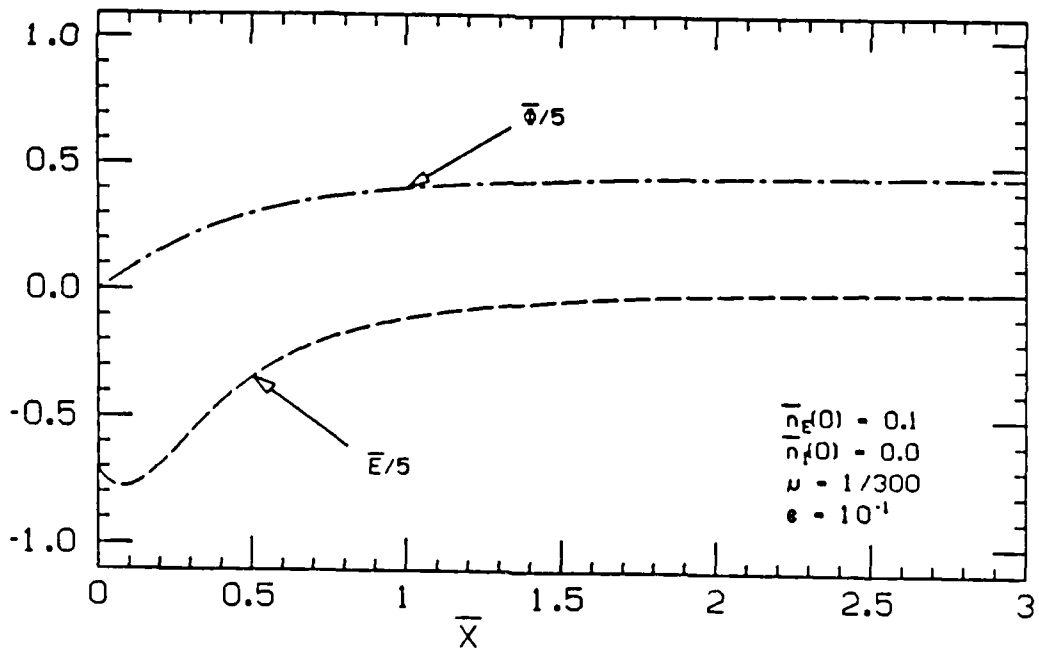
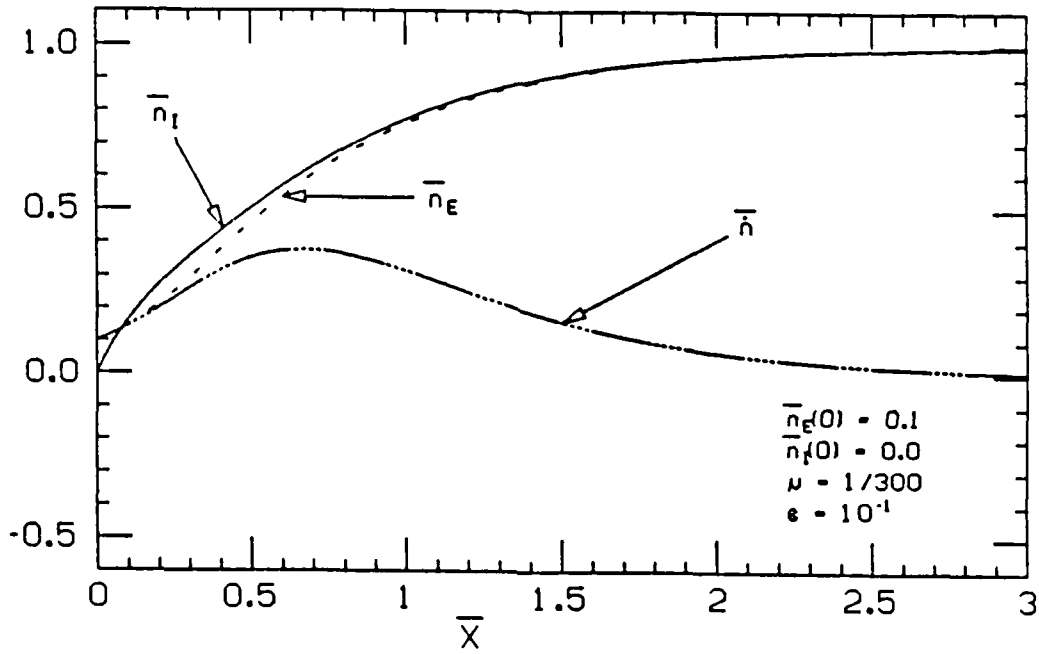


Figure 2.5. Profiles of: a) \bar{n}_e , \bar{n}_i , \dot{n} ; b) \bar{E} and $\bar{\Phi}$; parameter value $\mu = 1/300$, $\epsilon = 10^{-1}$, $\bar{J} = 0$, $\bar{n}_e(0) = 0.1$, $\bar{n}_i(0) = 0$.

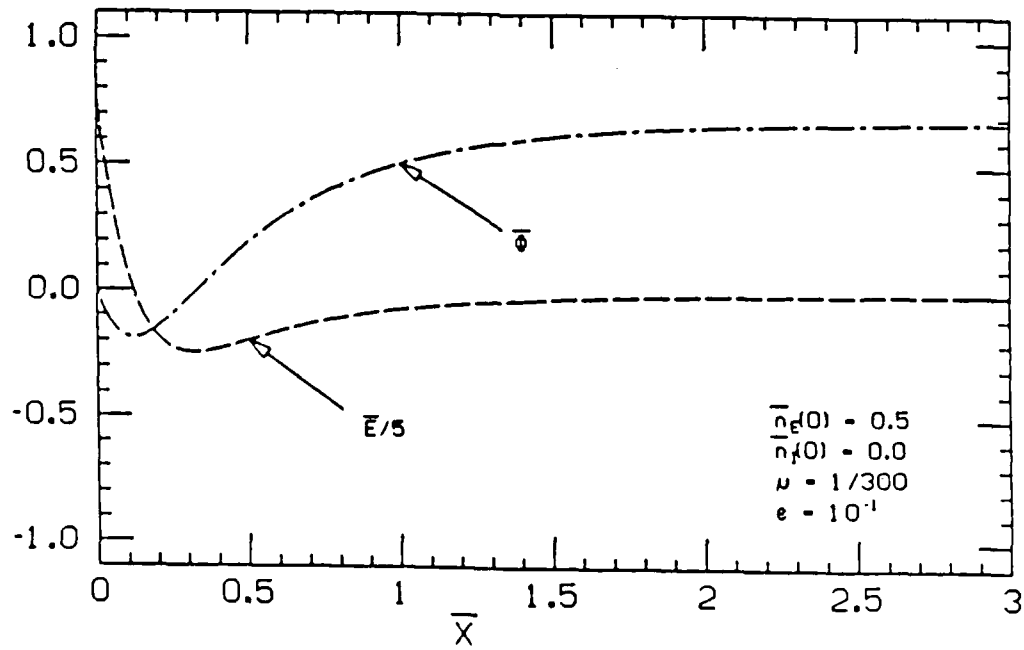
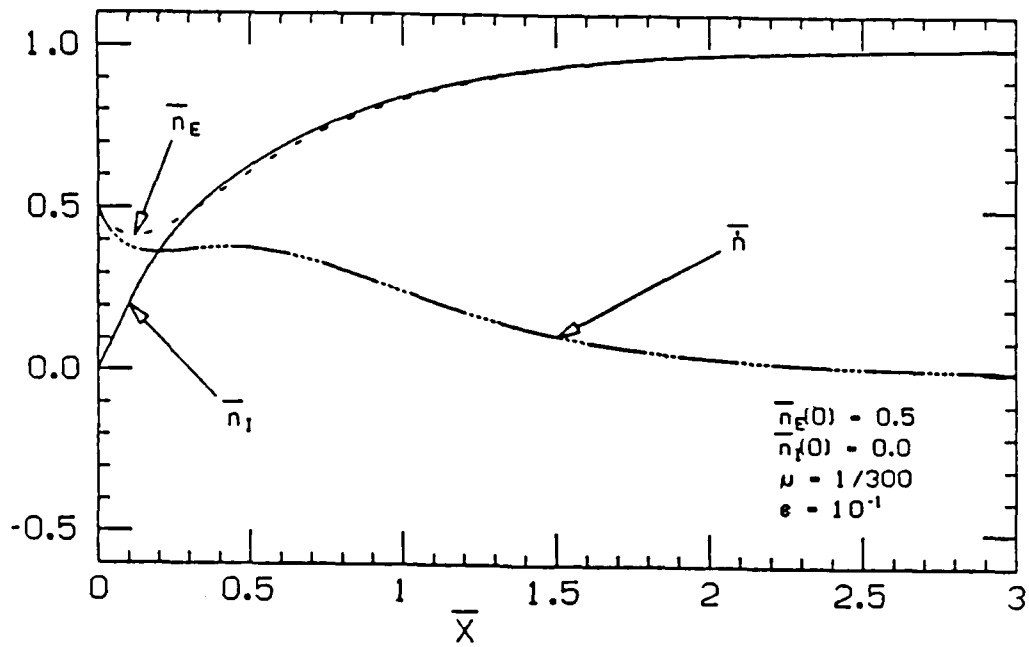


Figure 2.6. Profiles of: a) \bar{n}_e , \bar{n}_i , \bar{n} ; b) \bar{E} and $\bar{\phi}$; parameter values $\nu = 1/300$, $\epsilon = 10^{-1}$, $\bar{J} = 0$, $\bar{n}_e(0) = 0.5$, $\bar{n}_i(0) = 0$.

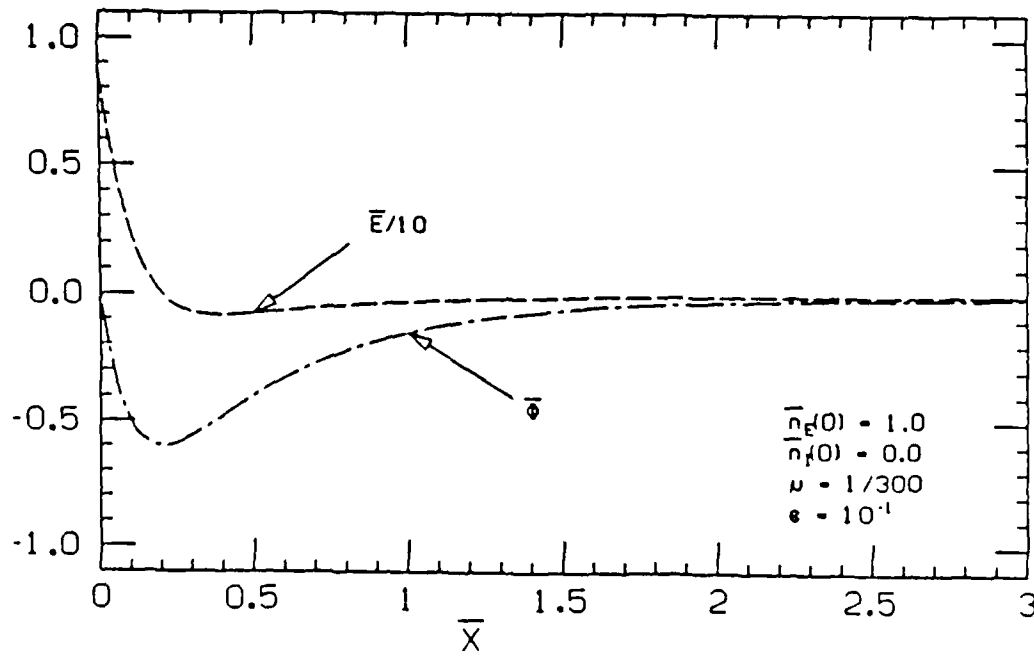
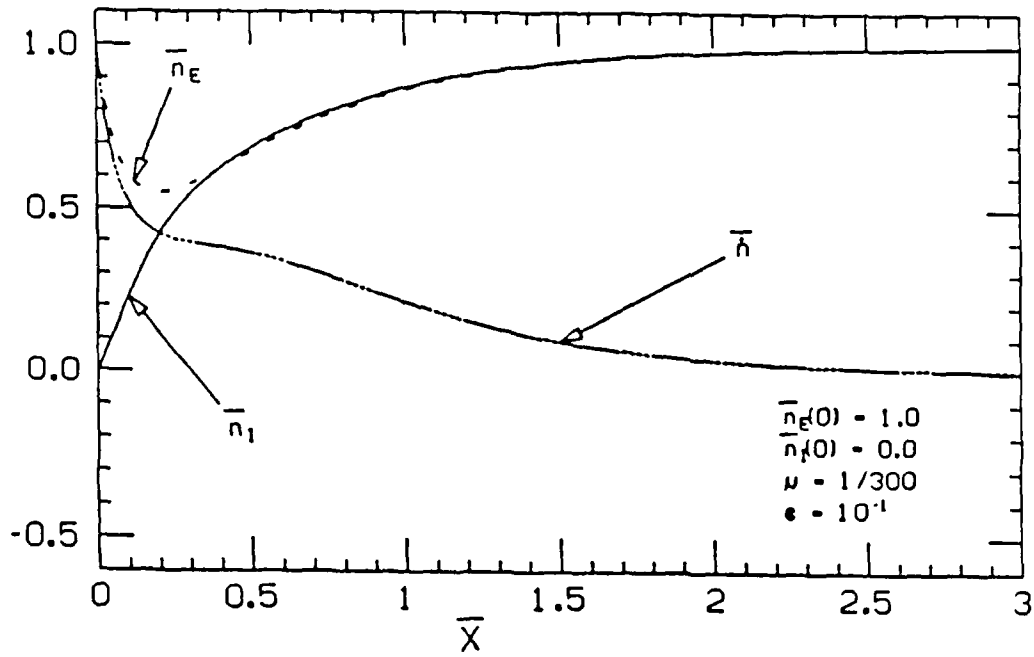


Figure 2.7 Profiles of: a) \bar{n}_e , \bar{n}_i , \bar{n} ; b) \bar{E} and $\bar{\phi}$; parameter values $\nu = 1/300$, $\epsilon = 10^{-1}$, $\bar{J} = 0$, $\bar{n}_e(0) = 1.0$, $\bar{n}_i(0) = 0$.

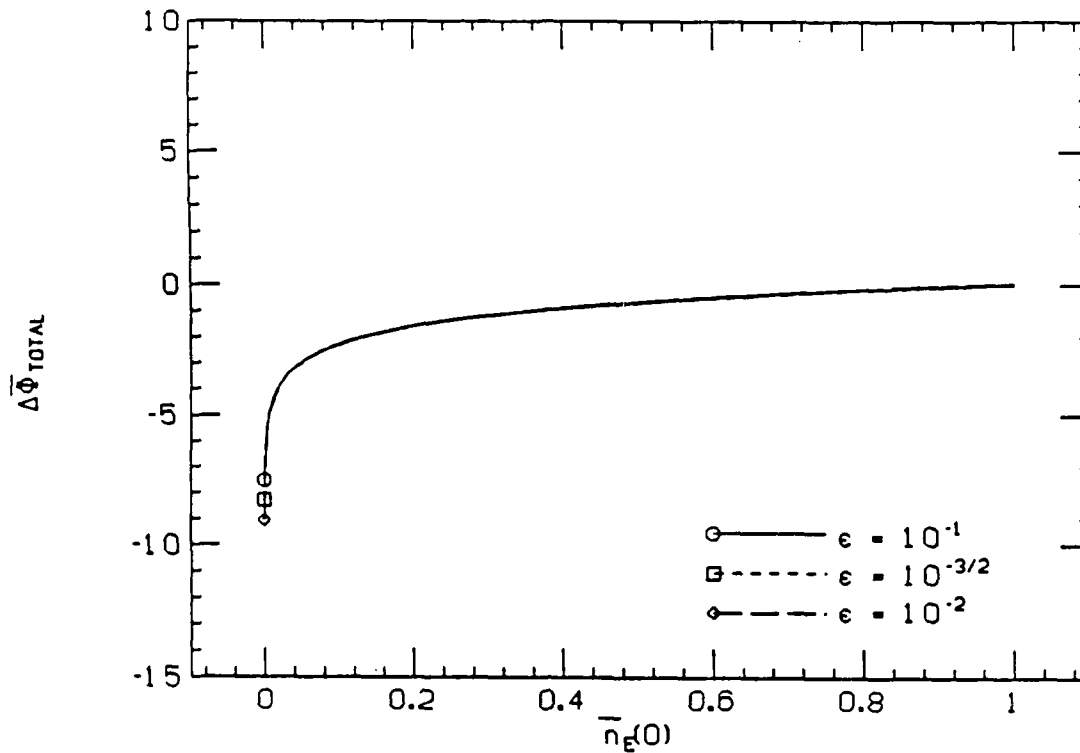


Figure 2.8. Total potential drop $\Delta\bar{\Phi}_{TOTAL}$ as a function of $\bar{n}_e(0)$, for various ϵ ; parameter values, $\mu = 1/300$, $\bar{J} = 0$, $\bar{n}_i(0) = 0$.

Experimental Work

The experimental work in progress is based on the use of a versatile bench-scale diffusion burner capable of producing a combustion plasma to 3000K. It is possible to seed the combustion products with 1% by mass of potassium vapor to produce a thermal plasma with a conductivity of up to 10 S/m. This facility was built in connection with an earlier NSF grant for the testing of plasma diagnostic techniques.

During the past contract year we have installed and partially configured a dedicated personal computer to be used for data acquisition. This machine (an Intel System 310) was donated by the Intel Corporation as part of an academic grant program.

We expect to measure the current-voltage characteristics and perform breakdown experiments during the current contract year.

2.3 Interaction of Discharges and Fluid Dynamics

Introduction

In several space power and propulsion systems of potential interest to the Air Force, such as MPD thrusters, MHD generators, and rail guns, fluid motions induced by discharges are of critical importance to both the understanding and performance of the system. The channel flow of a plasma through a transverse magnetic field is influenced by the Hall effect, which causes nonuniform Lorentz forces to arise in the direction mutually perpendicular to the channel axis and the magnetic field. These forces cause secondary flows to develop as the flow progresses down the region of electromagnetic-fluid interaction. The theoretical treatment of this problem has included the work of Fay [3.7], Broer, Peletier and Wijngaarden [3.4], Sato [3.18], Tani [3.20], Apollonskii and Kos'kin [3.1], Sastry and Bhadram [3.17], Liu, Lineberry and Schmidt [3.11], and Ishikawa and Umoto [3.9]. These secondary flows were predicted to be of substantial magnitude in the calculations reported by Maxwell et al [3.13], Bityurin, Zatelepin and Lyubimov [3.3] and Doss and Ahluwalia [3.6]. The calculated magnitude of these flows range from 10 to 30% of the bulk velocity, depending on conditions, and the predicted consequences include the development of significant asymmetries in the profiles of mean axial velocity and of temperature, with resultant effects on wall heat transfer and electrode voltage drops. In addition Demetriades et al [3.5] predicted that these secondary flows could lead to magnetoaerothermal instabilities, which could include boundary layer separation and/or electric field breakdown near the electrodes.

Indirect evidence for the existence of MHD-induced secondary flow, reviewed by Girshick and Kruger [3.8], included measurements of temperature profiles obtained by James and Kruger [3.10] and of electrode voltage drops obtained by Barton [3.2], which indicated that MHD effects caused the anode wall boundary layer of the channel to be colder than expected while the cathode wall is hotter than expected. It is hypothesized that these results could be ascribed to a secondary flow mechanism. Demetriades et al [3.5] conjectured that evident arc damage to the center of the anode wall in the downstream half of the channel used in

the High Performance Demonstration Experiment at the Arnold Engineering Development Center (Starr et al, 3.19) is a manifestation of the magnetoaerothermal instability mentioned above. McClaine, Swallow and Kessler [3.14] reported axial velocity profiles measured using a traversing stagnation pressure probe mounted in the diffuser of the Avco Mk VI generator. The profile measured between the top and bottom walls is found to be strongly skewed by MHD forces, presumably as a consequence of secondary flow.

Our current experiments provide the first direct, quantitative measurements of the secondary flow field in an MHD channel. Additionally, the effects of secondary flow on the plasma momentum, thermal and electrical behavior are being studied by making measurements of the profiles of mean axial velocity, turbulence intensity (axial and transverse) and plasma voltage, and by measuring electrode surface temperatures.

Research Objectives

The over-riding goal of our work in this area is to obtain experimental information which will allow us to describe the three-dimensional flow field in an MHD device. Specifically, the major objectives which presently guide this work are the following:

1. To study the effect of electromagnetic body forces on the secondary flow field. What are the magnitudes of these secondary flows, and how is their vortex structure affected by applied magnetic fields and discharges?
2. To study the effect of MHD interaction on mean axial velocity profiles. Are they affected by turbulence suppression caused by the magnetic field, and to what extent are they distorted by secondary flows?
3. To study the effect of MHD interaction on turbulence. What is the detailed nature of magnetic field turbulence suppression, including

the development of anisotropic turbulence? To what extent are turbulence intensity profiles distorted by secondary flows?

Status of Research

Theoretical Background

The fluid momentum equation for an MHD plasma can be written

$$\rho \frac{D\mathbf{u}}{Dt} = -\nabla p + \nabla \cdot \vec{\tau} + \mathbf{J} \times \mathbf{B} \quad (3.1)$$

where ρ is the mass density, p the thermodynamic pressure and $\vec{\tau}$ the viscous stress tensor. With $\mathbf{B} = B_z$, the presence of a non-zero Hall current causes the $\mathbf{J} \times \mathbf{B}$ Lorentz force to have a component in the y -direction. Taking the curl of (3.1) to obtain the fluid vorticity equation, we obtain for the axial vorticity Ω_x the result

$$\rho \frac{D\Omega_x}{Dt} = (\nabla \times \nabla \cdot \vec{\tau}) + B \frac{\partial J_x}{\partial z} \quad (3.2)$$

where we have assumed $B_z = \text{constant}$.

It is thus evident that the nonuniformity of the Hall current density between the core and the sidewalls introduces a rotational component into the Lorentz force. For the first-order profile of J_x pictured we would expect the two-cell flow structure shown on the right of Fig. 3.1 to arise. The presumed effect of such a secondary flow would be to transport hot, fast core plasma toward the bottom wall while sweeping relatively cold, slow sidewall fluid into the boundary layer of the top wall.

As the axial vorticity and the distribution of J_x are coupled through (3.2), the actual structure of the secondary flow field could be considerably more complicated than the simple pattern suggested in Fig. 3.1; indeed, J_x might not increase monotonically from the walls to the core, in which case the axial vorticity could change sign in some regions of the cross-plane. It should also be pointed out that Faraday

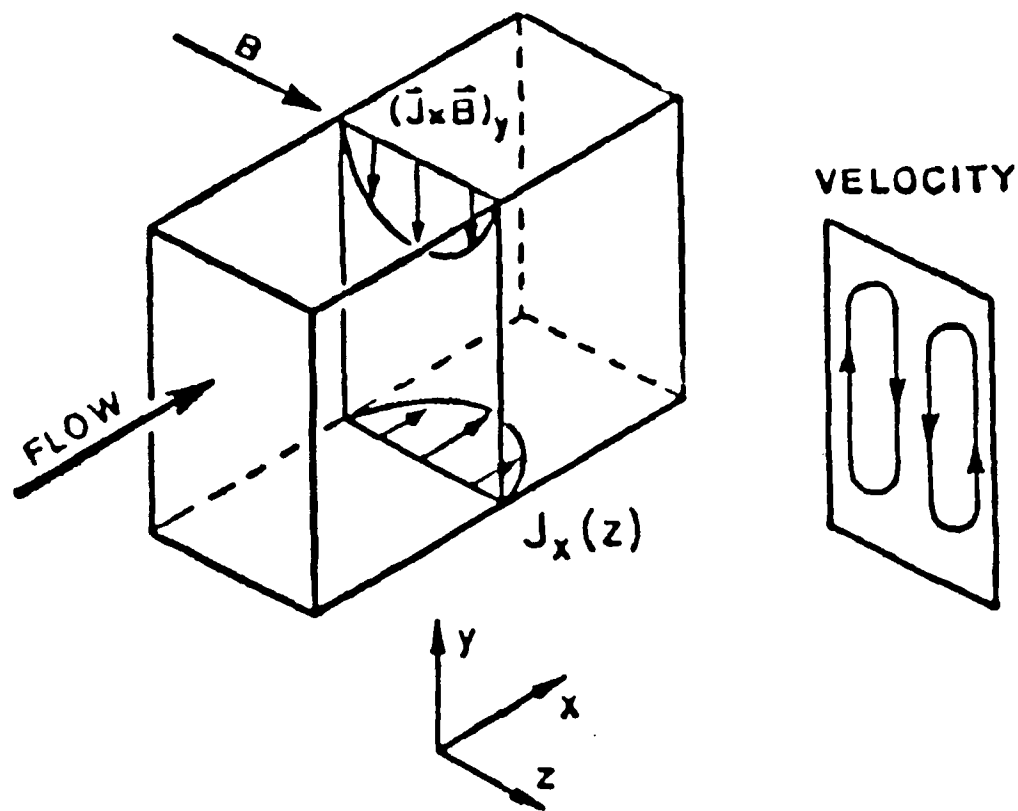


Figure 3.1 Secondary flow mechanism for a case of positive net Hall current.

MHD generators would suppress the flow of net Hall current by using segmented electrodes separated by insulators. However, the Hall effect would still cause the local value of J_x to be in general non-zero; only the integrated value of J_x over the cross-plane would vanish, and then only in the absence of axial leakage currents.

Description of experiments

Flow Train and Run Conditions

MHD secondary flow is being investigated in a series of experiments conducted at the High Temperature Gasdynamics Laboratory, with the M-2 flow train, shown in Fig. 3.2. This consists of a combustor with a

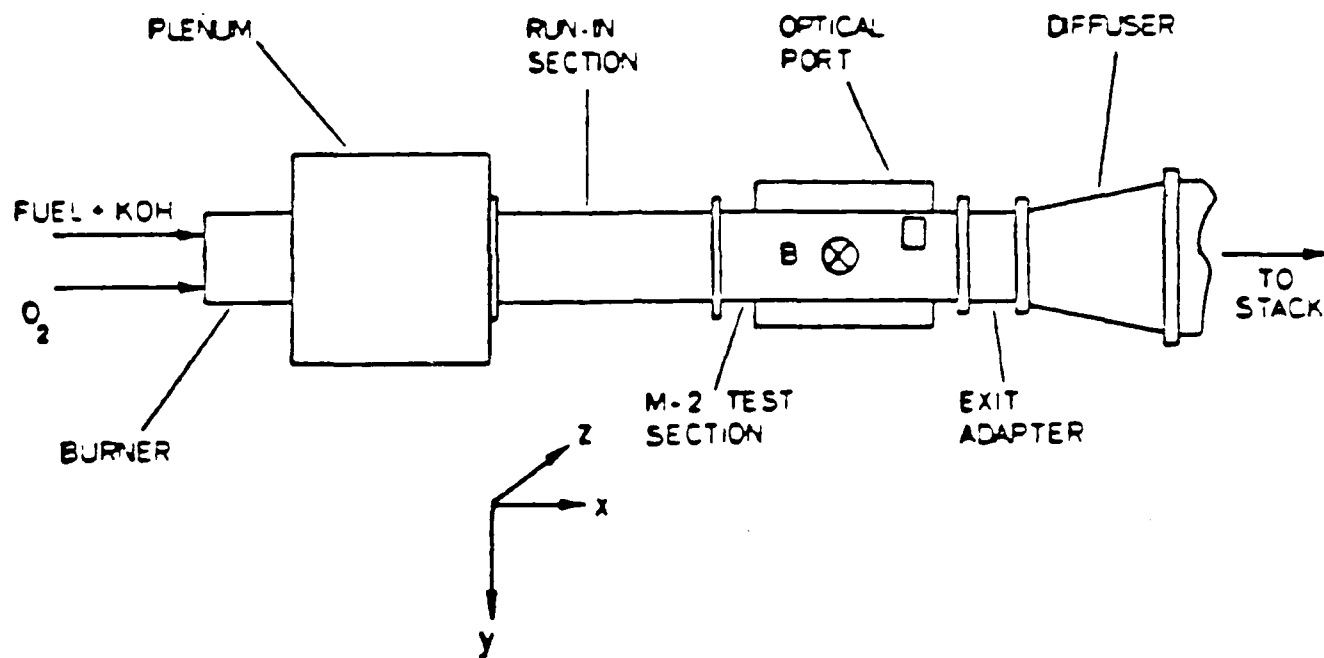


Figure 3.2 M-2 flow train.

nominal 2-MW thermal input rating, a large mixing plenum, a nozzle through which the combustion products are accelerated into a duct having a square cross-section measuring 5.1 cm on a side, a diffuser and an exhaust system including a scrubber and a stack. The square duct consists of a run-in section and the active channel itself, which is enclosed in a 2.6-T water-cooled, copper-coil magnet.

The plasma consists of the combustion products of ethyl alcohol (C_2H_5OH) burned in pure oxygen at a stoichiometry of 1.05 (fuel rich). The fuel is seeded with potassium hydroxide (KOH), such that potassium constituted 2.1% of the total products by mass. The total flow rate, 54.4 g/s, at a calculated nozzle exit temperature of 2750 K, corresponded to a Reynolds number (based on hydraulic diameter) of 1.3×10^4 ; the calculated nozzle exit velocity is 171 m/s. This value has been used throughout to characterize the bulk velocity U_b , although it should be noted that the actual bulk velocity decreases somewhat in the downstream direction as the plasma cools and becomes more dense. The flow thus

being turbulent, the boundary layers at the velocity measurement plane, which is 21.4 hydraulic diameters downstream of the nozzle exit, are fully developed (or at least nearly so) in the absence of MHD interaction.

Electrical Configuration

An important goal of the experiments has been to isolate the effect on the flow of the Hall current, since the Faraday current itself has important effects because it induces an axial Lorentz force given by $J_y B$. It is also considered desirable to establish conditions which allow insofar as possible for a straightforward interpretation of the measured secondary flow field. Accordingly the channel is connected in the "Hall configuration", with a pair of electrodes at the upstream end connected through an external load to a pair of electrodes at the downstream end, as shown in Fig. 3.3. A current of 9.3 amperes is driven through the plasma by means of a bank of batteries, and controlled by varying the load resistance. Thus the experimental situation corresponds to the case illustrated in Fig. 3.1, with a positive net Hall current.

A non-dimensional parameter which indicates the strength of the electromagnetic-fluid interaction is the Stuart number, or magnetic interaction parameter, S . For this configuration an appropriate definition of S is

$$S \equiv \frac{I_x BL}{\dot{m}U} \quad (3.3)$$

where I_x is the applied Hall current, L the distance from the first loaded electrode to the measurement plane, \dot{m} the mass flow rate and U the mean axial velocity. The interaction parameter in this form represents the ratio of the Lorentz twisting force to the axial inertia of the flow. The value of S in the present experiments is about 1.1 at the plane of the velocity measurements and slightly less at the measurement planes for conductivity and electrode temperature. This value is comparable to a similarly defined value based on the Hall current density in the core of a large-scale channel.

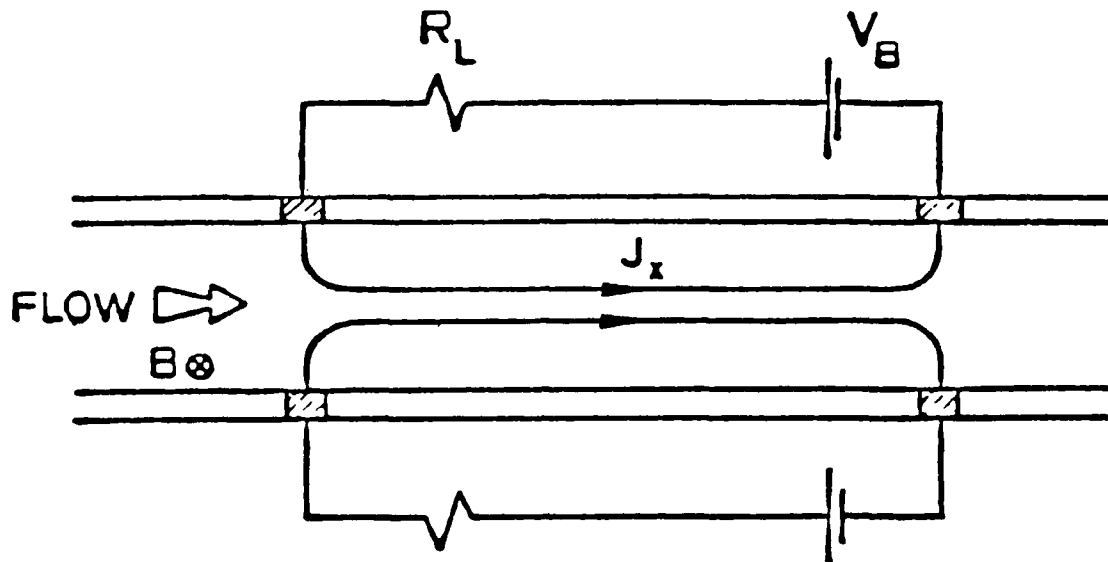


Figure 3.3 Electrical configuration used for the main experiments.

Laser Doppler anemometry system

Plasma velocities are measured using laser Doppler anemometry. The LDA system, shown schematically in Fig. 3.4, uses a dual-beam, single-color, backscatter configuration. Velocity measurements are made at numerous locations over the cross-plane defined by the port location. Translation of the measurement volume in the z -direction is achieved by translating the focusing lens along the optical axis, and in the y -direction by rotating about its horizontal axis a large mirror which directs the converging beams toward the small mirror next to the optical port.

Conductivity measurements

The effect of secondary flow on the plasma conductivity profile is investigated by driving a Faraday discharge across a set of electrodes whose external circuitry is separate from that used to drive the Hall current. This set consists of three electrode pairs located just upstream of the optical port. These electrodes are used only for the conductivity measurements, and are open-circuited at all other times. The outer two pairs serve as guard electrodes, so that the Faraday current density J_y flowing across the gap of the middle pair can be estimated more accurately. Near-electrode voltage drops in both the

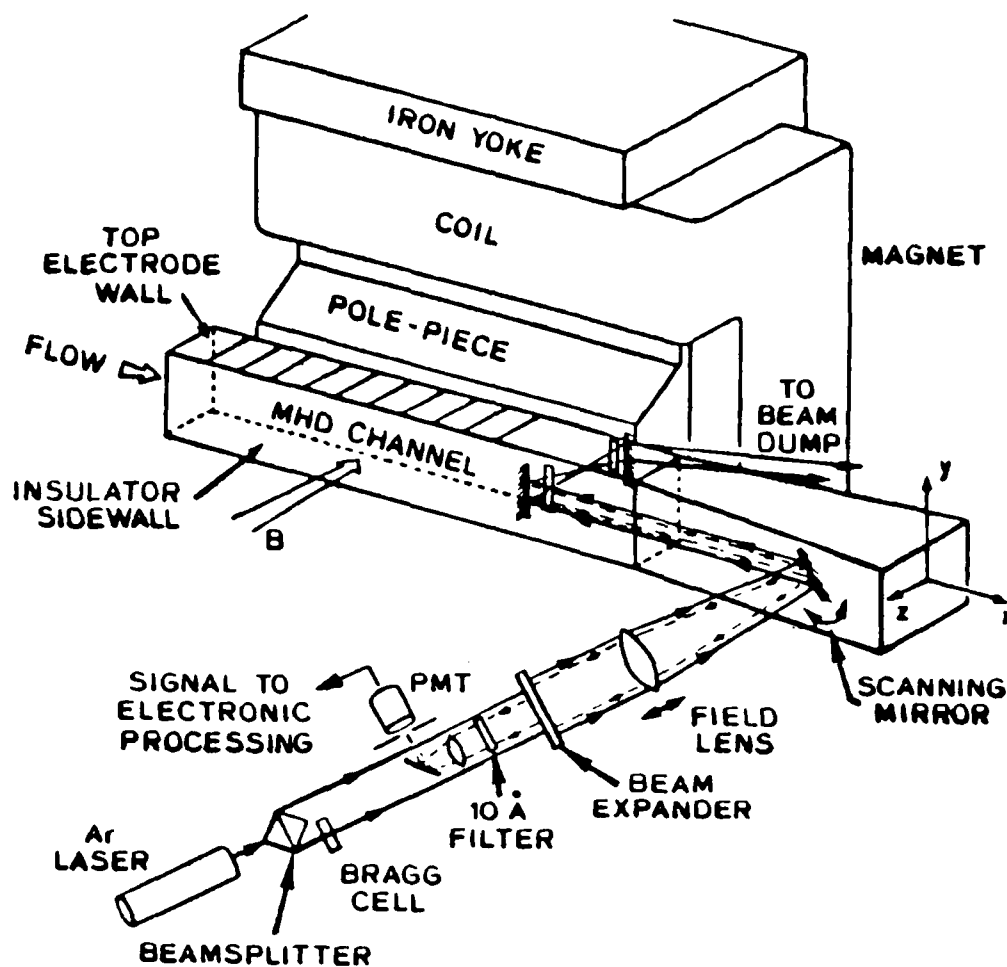


Figure 3.4 Schematic of laser Doppler anemometry optical train.

x- and y-directions are obtained from a grid of iridium voltage pins inserted through a channel sidewall. Voltage distributions are obtained over a range of values for J_y , and under various applied conditions, including:

1. applied Faraday current only;
2. both Faraday current and Hall current;
3. Faraday current with magnetic field; and
4. Faraday current, Hall current and magnetic field.

For cases (3) and (4) measurements are made with the magnetic field pointing in both the positive- and negative-z directions. The open-circuit voltage with magnetic field is measured as well. Note that only case (4) would be expected to drive secondary flow.

The voltage information is analyzed using an approximate model based on the expression, obtainable from the generalized Ohm's law,

$$\bar{\rho} = \frac{\overline{E_y} - \overline{uB} + \beta \overline{E_x}}{(1 + \beta^2) J_y} \quad (3.4)$$

where ρ is the resistivity, E_y and E_x the electric field components and u the axial velocity. The overbar indicates an average over a region of the cross-plane which encompasses the width W in the z -direction and ranges in the y -direction from the electrode surface to the height of the nearest voltage pin, a distance of 6.2 mm, or $H/8$, H being the channel height.

Temperature measurements

All electrodes are fitted with thermocouples located close to their surfaces. Of particular interest are the temperatures of the electrode pair just upstream of the velocity measurement plane, for cases in which these electrodes are not passing current. A number of measurements are recorded for runs in which a case without secondary flow (i.e., without the simultaneous presence of magnetic field and Hall current) is immediately followed or preceded by a case with secondary flow (i.e., both were present). The change in surface temperature between these two cases can then be attributed to altered heat transfer as a result of secondary flow. As with the other measurements, data is collected for both the positive- and negative- z orientations of the magnetic induction.

Experimental results

Transverse velocity measurements

Non-MHD case

So as to have a base case with which to compare the measurements with MHD effects present, measurements of the y-directed velocity have been made for the case of zero magnetic induction and zero current. The results are shown in Fig. 3.5. The peak measured transverse velocity is $0.05 U_b$. This is significantly higher than reported measurements for secondary flows driven purely by the interaction of turbulence stresses with the corners of a rectangular duct. Several factors may be involved in this discrepancy, including combustion non-uniformities and other non-idealities related to the combustor, density gradients, and the heterogeneous nature of the channel walls (the top and bottom walls had alternating sections of brick and of electrodes, whereas the sidewalls had only brick).

MHD cases

Measurements of the y-directed velocity have been made for a range of conditions, and with the magnetic field pointing in both the positive- and negative-z directions. Reversing the magnet polarity reverses the sign of the Lorentz force, and so should be approximately equivalent to rotating the channel by 180° about its axis.

The measurements for the case of \mathbf{B} pointing in the positive-z direction are shown in Fig. 3.6. In this figure and in the figures following the secondary flow appears stronger near the left sidewall than near the right; we believe that this is an artifact caused by a consistently erroneous measurement of the wall location. Shifting all the measurement locations to the left by an amount $\Delta(z/W) = 0.035$ would produce a symmetric result, which is physically what we would expect. This systematic error is additional to the uncertainty in spatial location.

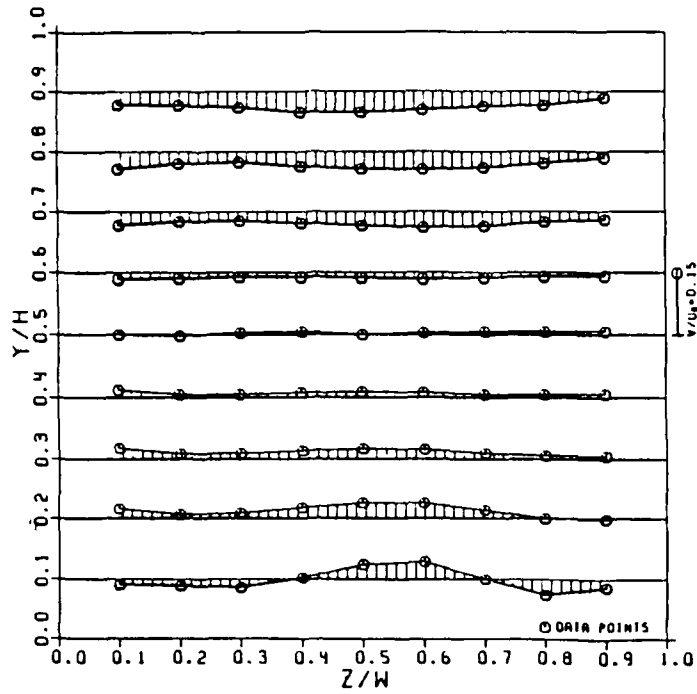


Figure 3.5 Measurements of the mean y-directed velocity without magnetic field.

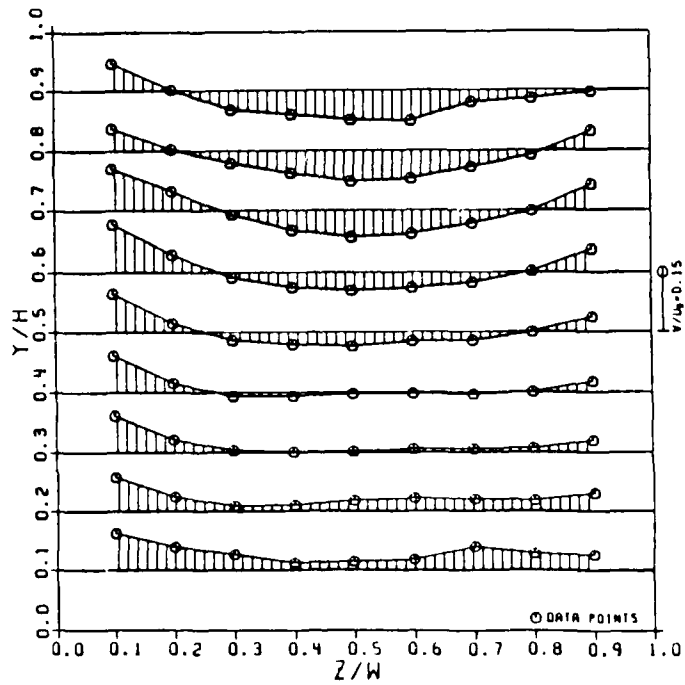


Figure 3.6 Measurements of the mean y-directed velocity with the magnetic field pointing in the positive z-direction.

In any case, the results suggest the presence of two large, counter-rotating secondary flow cells, with the flow in the core directed downward in agreement with the first-order argument illustrated in Fig. 3.1. The peak measured velocities, found in the sidewall region, measured $0.12 U_b$; as the magnitude of the transverse velocity is increasing steeply toward the sidewall, it is reasonable to assume that significantly higher velocities would be found by measurements closer to the walls.

The vorticity is concentrated in the top half of the channel, with the vortex cells closing at about $y/H = 0.35$. An explanation for this behavior is suggested by a three-dimensional numerical simulation performed by Maxwell, Early and Demetriades [3.12] for conditions which were similar to those of the present experiments. In these calculations the secondary flow field at the upstream end of the interaction region has a symmetric structure similar to that in Fig. 3.1. As the flow progresses, hot plasma from the core has time to be swept sideways and then upwards as it follows a secondary flow path. This has the effect of increasing $\partial J_x / \partial z$ in the upper sidewall regions, which in turn intensifies the vorticity in these regions. The coupling between $\partial J_x / \partial z$ and axial vorticity causes the secondary flow cells to migrate toward the top walls in the downstream half of the channel. In this respect the simulation and the measurements are in good agreement. The quantitative agreement is also reasonably good, although precise comparisons would require a more detailed specification than is available of the sidewall temperature distributions and of the upstream turbulence history. Both of these factors were shown in the simulation to have a substantial influence on the secondary flow field: the sidewall temperature because it affects $\partial J_x / \partial z$, the turbulence intensity because of its cross-plane smoothing effect.

The measurements in the region at the bottom of the cross-plane indicate a flow which is everywhere directed away from the bottom wall. A possible explanation for these measurements is discussed in connection with the temperature results.

In Fig. 3.7 the results for the case with the magnet polarity reversed are shown. As anticipated the velocity field is upside-down compared to the results in Fig. 3.6. A few measurements have been made in this case closer to the sidewalls, resulting in a peak transverse velocity measurement of $0.15 U_b$.

Effects of Secondary Flow

The measured secondary flow field is certainly strong enough to have an effect on several aspects of the plasma momentum and thermal behavior. This section reports the results of the measurements of mean axial velocity, turbulence intensity, electrical conductivity and electrode surface temperature.

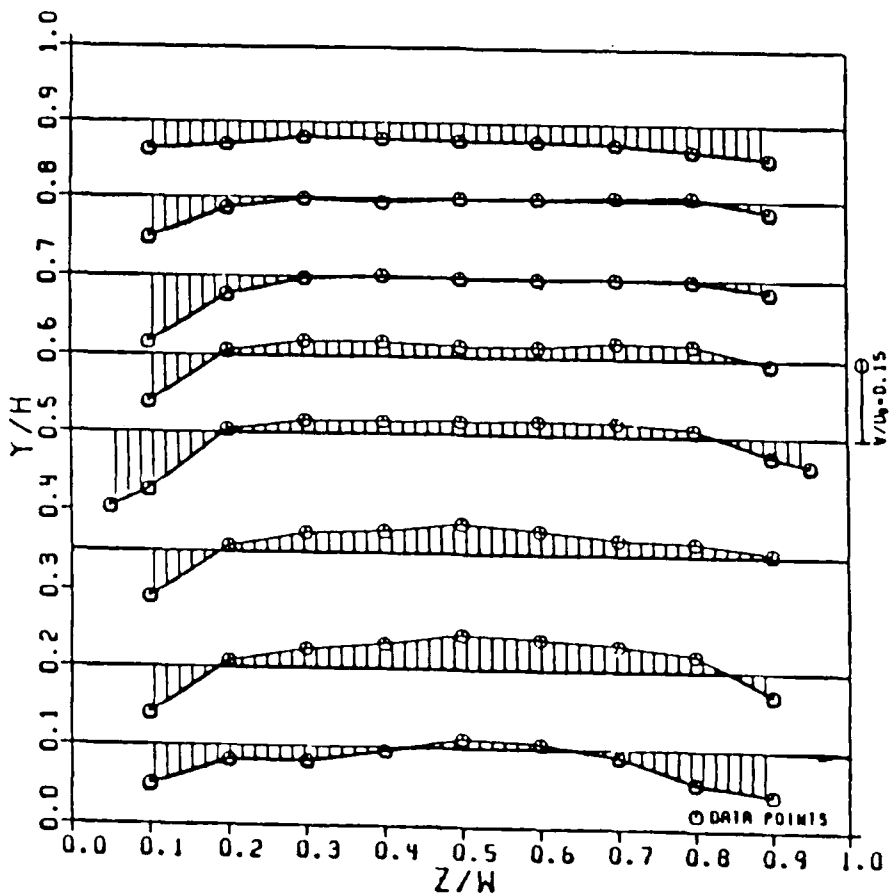


Figure 3.7 Measurements of the mean y-directed velocity with the magnetic field point in the negative z-direction.

Mean axial velocity

Measurements of the mean axial velocity with the magnetic field pointing in the positive-z direction are shown in Fig. 3.8; these results correspond to the secondary flow field shown in Fig. 3.6. The distortion of the velocity profile is dramatic: the peak velocity is forced downward from the center of the cross-plane to a position of about $y/H = 0.3$. The isovels near the top wall follow the vortex pattern, as slow-moving fluid is swept upward along the sidewall and then pushed downward along the z-centerline. The axial velocity profiles along the z-centerline for three conditions of the magnetic field are shown in Fig. 3.9. As expected the profile is symmetric when Lorentz forces were absent; with Lorentz forces present the profile became strongly skewed according to the direction of the force.

These results are similar to the measurements reported by McClaine, Swallow and Kessler [3.14]. In their experiments, performed in the larger Avco Mk VI channel, the conditions included a magnetic induction of 4 T, an interaction length of 2.5 m, and peak velocities of about 1000 m/s. Unfortunately the electrical loading which is used during these particular measurements is not reported; their tests encompassed a wide range of loading conditions in both Faraday and diagonal configurations.

Turbulence intensity

Previous measurements of turbulence intensity in the Stanford M-2 channel have found relatively high values of the center-point axial turbulence intensity \tilde{u}_c/\bar{u}_c , where \tilde{u}_c is the turbulence velocity (the standard deviation of the velocity probability distribution function) and \bar{u}_c is the center-point mean velocity. For example, Reis and Kruger [3.16] measured values ranging from 6.6% to 9.6% for a variety of non-MHD flow cases; in the present experiments several measurements of \tilde{u}_c/\bar{u}_c yielded values ranging from 5.8% to 6.3%. For comparison, Melling and Whitelaw [3.15] in their water flow experiment measured

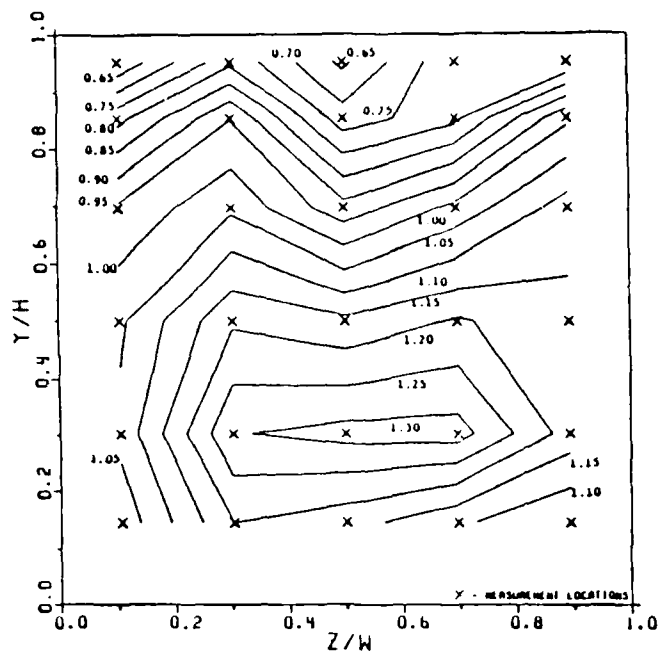


Figure 3.8 Contour map of the measured mean x-directed velocity (normalized by U_b) with the magnetic field point in the positive z-direction.

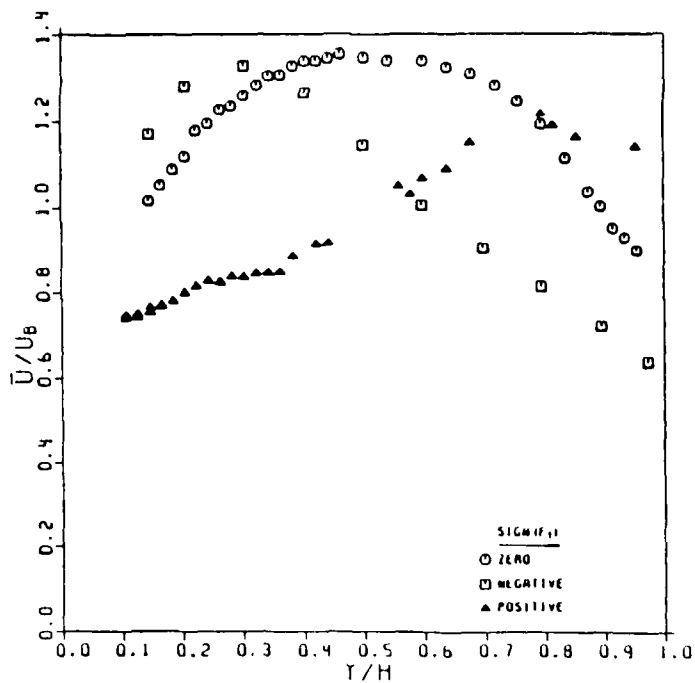


Figure 3.9 Measurements of the mean x-directed velocity along the z-centerline, for three conditions of the transverse Lorentz force F_y .

values of 4-5% at an axial location where the boundary layers had merged. It has been conjectured that the relatively high axial turbulence in the Stanford channel is caused by combustion nonuniformities. The measured value in the non-MHD case of the y-directed core turbulence \tilde{v} , again normalized by \bar{u}_c , is 3.75%; this is virtually identical to the value reported by Melling and Whitelaw [3.15].

Measurements of the y-directed turbulence intensity in the non-MHD case are shown in Fig. 3.10, in which the measured values of \tilde{v} have been normalized by U_b . As expected the distribution is symmetric and $|\tilde{v}|$ is greater near walls parallel to y than near walls normal to y.

The measurements made in the MHD case, with the magnetic field pointing in the positive-z direction, are shown in Fig. 3.11. The region of minimum turbulence (whose magnitude is somewhat less than in the non-MHD case because of turbulence damping by the magnetic field; cf. Reis and Kruger [3.16]) is shifted downward by Lorentz forces.

The measurements for \tilde{u}/U_b , shown in Fig. 3.12, exhibited the same effect; these same measurements are shown in Fig. 3.13 normalized instead by the local mean velocity \bar{u} . In these measurements there appears to be a region beneath the center of the top wall where the turbulence is greater than its value closer to the wall; this might be explainable in terms of secondary flow convection.

Electrical conductivity

The results of the conductivity measurements for the MHD cases are summarized in Fig. 3.14, in which the near-electrode resistivity defined by equation (6) has been normalized by the value of the core conductivity measured without magnetic field. The terms "anode region" and "cathode region" refer respectively to the regions adjacent to the top and bottom electrodes which were used for the conductivity measurements. The abscissa in this figure represents the value of the core current density associated with the Faraday discharge; for all the data shown the Hall circuit is active as well, corresponding to case (4) described earlier.

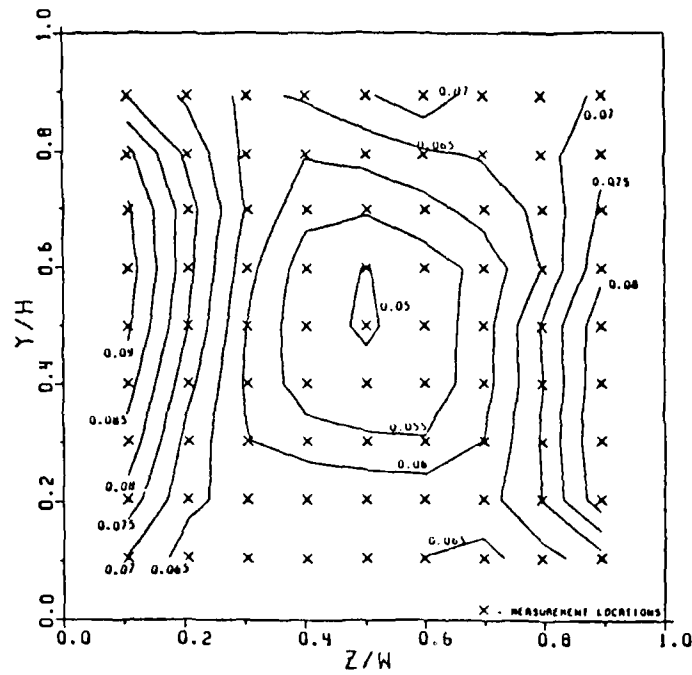


Figure 3.10 Contour map of the measured y-directed turbulence intensity (normalized by the bulk axial velocity) without magnetic field.

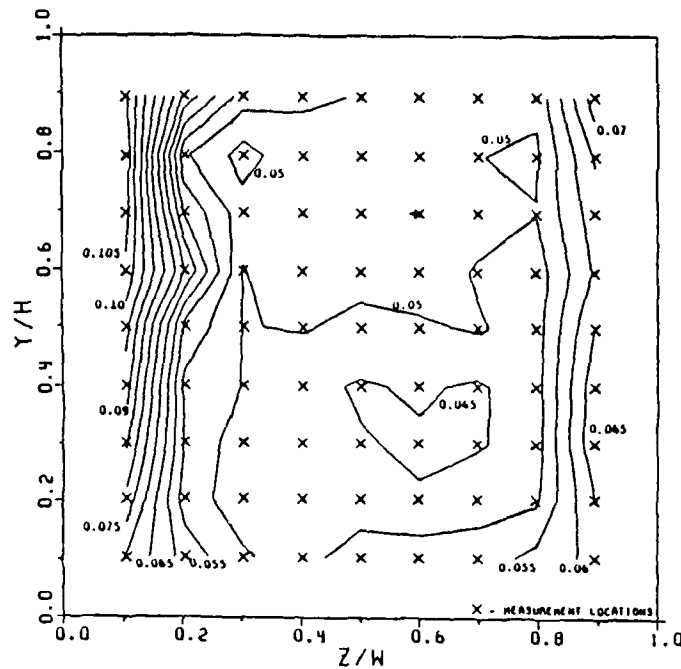


Figure 3.11 Contour map of the measured y-directed turbulence intensity (normalized by the bulk axial velocity) with the magnetic field pointing in the positive z-direction.

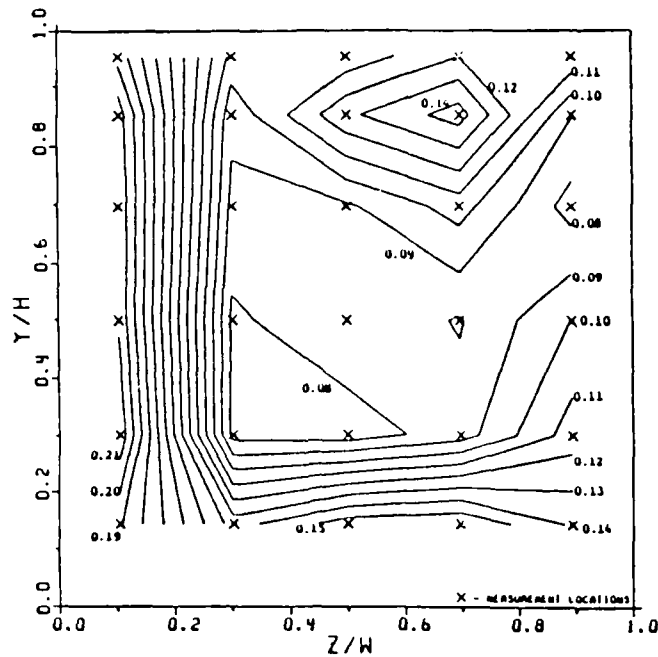


Figure 3.12 Contour map of the measured x-directed turbulence intensity (normalized by the bulk axial velocity), with the magnetic field pointing in the positive z-direction.

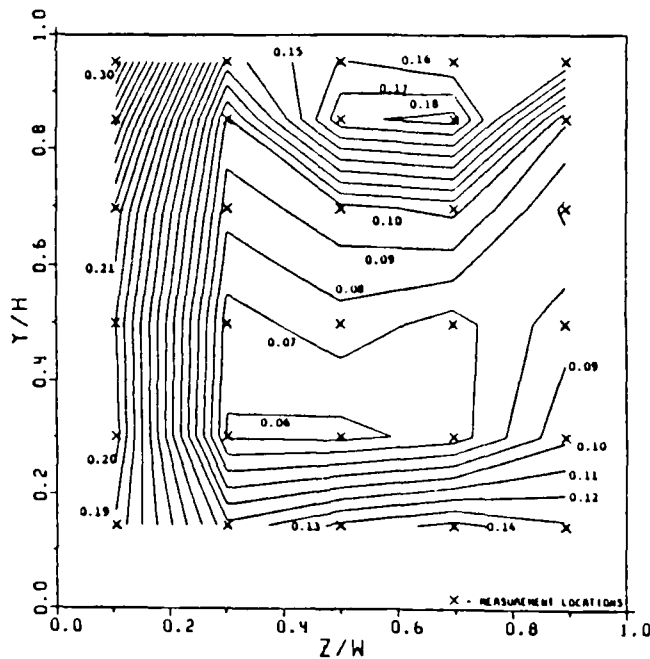


Figure 3.13 Contour map of the measured x-directed turbulence intensity (normalized by the local mean axial velocity) with the magnetic field pointing in the positive z-direction.

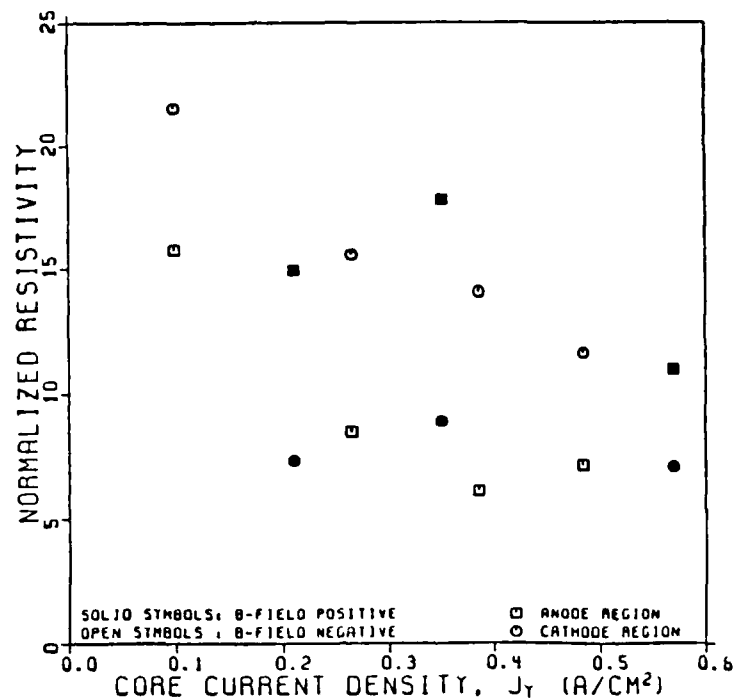


Figure 3.14 Summary of resistivity results for cases with complete electrical configuration and magnetic field.

The decrease in resistivity as J_y increased is an expected consequence of Joule heating. Otherwise these results indicate that secondary flow caused the resistivity distribution to become significantly asymmetric. The boundary layer receiving cold sidewall fluid is much more resistive than the boundary layer toward which hot core fluid is directed; the average value of the ratio of the higher resistivity to the value at the opposite wall is 1.8. The importance of these results is that near-electrode voltage drops, which are a performance-limiting effect in combustion MHD devices, can be significantly altered by secondary flow.

Electrode Surface Temperatures

Thirteen separate measurements have been made of the effect of secondary flow on electrode surface temperatures, as described earlier. The results are shown in Fig 3.15. Each point in this figure represents

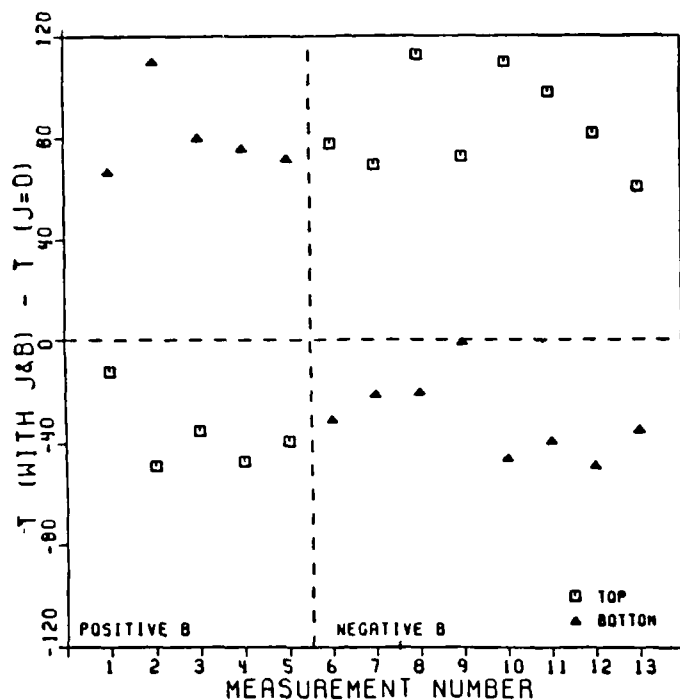


Figure 3.15 Measured electrode surface temperatures with Hall current and magnetic field minus reference measurements without current.

the temperature with secondary flow (with simultaneous Hall current and magnetic field) minus the temperature without secondary flow (without current); the latter temperature is typically about 1000 K. A separate analysis of data not shown in the figure indicates that the presence of magnetic field alone makes no difference in the temperature, while the presence of Hall current alone causes a warming of both the top and bottom electrodes by an average of about 10 K, because of Joule heating.

The effect of secondary flow in the positive-B case is seen to be a substantial heating of the bottom electrode and a smaller but still significant cooling of the top electrode; reversing the magnet polarity reversed the results. The electrode toward which hot core fluid is pushed is heated on the average by 85 K; the opposite electrode is cooled by an average of 32 K. Using the fact that the electrodes are cooled by water at about 300 K, we calculate that secondary flow evidently causes a 12% increase in the heat flux from the plasma to the heated electrode and a 5% reduction in the heat flux to the cooled electrode.

Aside from the obvious conclusion that secondary flow has the expected qualitative asymmetric effect on heat transfer to the top and bottom walls, it is interesting to consider the surprising result that the effect at the heated electrode is more than twice as great as the effect at the cooled electrode. This result is surprising, first, because the secondary flow cells appear to be concentrated near the cooled electrode, and second, because the resistivity measurements show the opposite trend, with a stronger effect being observed in the region adjacent to the cooled electrode.

A possible explanation is as follows. As already noted, the secondary flow cells not only sweep cold sidewall fluid into the top wall boundary layer, but also eventually convect hot core fluid around a loop into the same boundary layer in the sidewall region. As the stainless steel electrodes are thermally quite conductive, the net result is that the cooling effect is mitigated; no such effect occurs for the boundary layer of the bottom wall, toward which core fluid has been pushed but which has less vortical mixing. Distortion of the turbulence distribution could also be a factor in the asymmetrical heat transfer. Near-electrode voltage drops, on the other hand, are dependent on complex physical processes which are strongly but non-linearly temperature-dependent. Since the calculated resistivities have been averaged over an area described earlier, it is not remarkable that the net quantitative effects for the resistivity distribution could be quite different than for heat transfer, although the qualitative trends are the same.

The temperature results suggest a possible explanation for the secondary flow measurements in the region near the bottom wall (in the positive-B case). The substantial warming of the bottom electrode suggests that the mass density near the bottom wall may have been decreasing in the axial direction, causing a net reduction in the axial mass flux which would have to be balanced by a flow away from the wall. Although this behavior did not appear in the simulation of Maxwell, Early and Demetriades [3.12], their calculations assumed that the wall temperature is constant.

Conclusions

In conclusion, the past year has been one of significant achievement for our program in MHD-induced secondary flow. The results constitute the first direct, quantitative measurements of secondary flow in a combustion MHD channel. Our experiments are showing that strong secondary flows can be driven by Lorentz forces which are present in moderate-to high-interaction MHD devices, and that these secondary flows can have a profound impact on the performance of these devices.

3.0 REFERENCES

- 1.1 Mitchner, M. and C.H. Kruger, Jr., "Partially Ionized Gases," John Wiley & Sons, Inc., 1973.
- 1.2 James, R.K., "Joule Heating Effects in the Electrode Wall Boundary Layer of MHD Generators," HTGL Report No. 115, Stanford University, January 1980.
- 1.3 Bates, D.R., V. Malaviya and N.A. Young, "Electron-Ion Recombination in a Dense Molecular Gas," Proc. Roy. Soc., A-320, p. 437, (1971).
- 1.4 Roth, A., Vacuum Technology, North Holland, 1976, p. 156.
- 1.5 Ibid., p. 144.
- 1.6 Doucet, H., A. Truc, and A. Richardt, "Piegeage des vapeurs d'eau et d'oxygene dans une enceinte en haut vide et en vide clasique", Le Vide, 132, p. 347, (1967).
- 1.7 Spears, K.G., "Ion-Neutral Bonding", Journal of Chemical Physics, 57, p. 1850, (1972).
- 1.8 Dzidic, J., and P. Kebarle, "Hydration of the Alkali Ions in the Gas Phase. Enthalpies and Entropies of Reactions $M^+(H_2O)_{n-1} + H_2O = M^+(H_2O)_n$ ", Journal of Physical Chemistry, 74, p. 1466, (1970).
- 1.9 Hinnoy, E, and J.G. Hirschberg, "Electron-Ion Recombination in Dense Plasmas", Phys. Rev., 125, p. 795, (1962).
- 1.10 Patrick, R., and D.M. Golden, "The Temperature Dependence of Ion-molecule Association Reactions", J. Chem. Phys., 82, p. 75, (1985).
- 1.11 Franklin, J.L. ed., Ion-Molecule Reactions, Dowden, Hutchinson, and Ross, (1979).
- 1.12 Vincenti, W.G., and C.H. Kruger, Jr., Introduction to Physical Gas Dynamics, Krieger, p. 144, (1965).
- 1.13 Ibid., Chapter IV.
- 1.14 Ibid, p. 524.
- 1.15 Stogryn, D.E., and A.P. Stogryn, Mol. Phys., 11, p 371, (1966).
- 1.16 Searles, S.K., and P. Kebarle, "Hydration of the Potassium Ion in the Gas Phase: Enthalpies and Entropies of Hydration Reactions $K^+(H_2O)_{n-1} + H_2O = K^+(H_2O)_n$ ", Can. J. Chem., 47, p. 2619, (1969).

- 1.17 Niles, F.E., J.M. Heirmerl, G.E. Keller, and L.J. Puckett, "Reactions Involving Cluster Ions", Radio Science 7, p. 117, (1972).
- 1.18 Janaf Thermochemical Tables, second edition, NSRDS-NBS-37, (1971).
- 1.19 Loeb, L.B., Basic Processes of Gaseous Electronics, p.590, Univ. of Cal. Press, (1955).
- 1.20 Clifton, D.G., "Ideal Gas Treatment of the Equilibrium Composition, Enthalpy Function, and Heat Capacity of Cesium Vapor and Cesium Plasma", Los Alamos Report LA-2419, p. 13, (1960).
- 1.21 Harris, L.P., J. Appl. Phys., 36, p.1543, (1965).
- 1.22 McGowan, J.Wm., and J.B.A. Mitchell, "Electron-Molecular Positive-Ion Recombination", in Christophorou, L.G., ed., Electron-Molecule Interactions, Vol.2, p. 65, (1984).
- 1.23 Ditchburn, R.W., "The Absorption of Light in Cs Vapour in the Presence of Foreign Gases", Proc. Roy. Soc., A157, p 66.
- 1.24 Welty et al., Fundamentals of Momentum, Heat, and Mass Transfer, 1976, p. 566.
- 1.25 Nygaard, K.J., "On the Effect of Cs in Photoionization Laser Plasmas," IEEE J. Quantum Electronics, QE-9, P1020.
- 1.26 Trenholme, J.B. and J.L. Emmett, "Ultraviolet Output from Pulsed Short Arcs," Naval Research Lab, NRL-NR-2427, (1972).
- 1.27 Hodgson, B.W. and J.P. Keene, "Some Characteristics of a Pulsed Xe Lamp," Rev. Sc. Instr., 43, p. 493, (1972).
- 1.28 Hower, N.L., "Measurements of Electrical Conductivity of MHD Plasmas with Four-Pin Probes," Stanford HTGL Scientific Report No. 108, February 1978.
- 1.29 Houben, J.W.M.A., "Loss Mechanisms in a MHD Generator," Thesis Eindhoven Univ. of Tech., (1973).
- 1.30 Borghi, C.A., "Discharges in the Inlet Region of a Noble Gas MHD Generator," Thesis Eindhoven Univ. of Tech., (1982).
- 1.31 Keller, G.E., and R.A. Beyer, "CO₂ and O₂ Clustering to Sodium Ions", J. Geophysical Res., 76, p. 289 (1971).
- 1.32 Hirschfelder, Molecular Theory of Gases and Liquids, Wiley, 1954, p. 946.
- 1.33 Slater et al, Phys. Rev. A, 17, p. 201 (1978).

- 2.1 Pfender, E., "Electric Arcs and Arc Gas Heaters", in Gaseous Electronics, Volume 1: Electrical Discharges, Hirsch, M. N. and Oskam, H. J., (Eds.), Academic Press, 1978, pp. 291-398.
- 2.2 Hernberg, R., "Boundary Layer Breakdown and Discharges on Copper Cathodes in a Partially Ionized Molecular Gas", PhD Thesis, Tampere University of Technology, 1983.
- 2.3 Eskin, L. D. and S.A. Self, "Plasma-Sheath Structure for an Electrode Contacting an Isothermal Plasma: I. Formulation and Quasi-neutral Solution", Submitted to Phys. Fluids, 1985.
- 2.4 Eskin, L. D. and S.A. Self, "Plasma-Sheath Structure for an Electrode Contacting an Isothermal Plasma: II. An Electrically Isolated (Floating) Electrode", Submitted to Phys. Fluids, 1985.
- 3.1 Apollonskii, S.M. and Yu. P. Kos'kin, "On Transverse Velocity Disturbances in Magnetohydrodynamic Channel Flows," Magnetohydrodynamics 4, 37. 1968.
- 3.2 Barton, J.P., "Fluctuations in Combustion Driven MHD Generators," Ph.D. Dissertation and HTGL Report No. 118, Stanford University, 1980.
- 3.3 Bityurin, V.A., V.N. Zatelepin, and G.A. Lyubimov, "Effect of Force Field Nonuniformity on Flow in an MHD Channel," Fluid Dyn. 13, 1, 1978.
- 3.4 Broer, L.J.F., L.A. Peletier, and L. van Wijngaarden, "A Mechanical Hall Effect," Appl. Sci. Res., Sect. B. 8, 259, 1960.
- 3.5 Demetriades, S.T., D.A. Oliver, T.F. Swean and C.D. Maxwell, "On the Magnetoaerothermal Instability," AIAA 19th Aerospace Sciences Meeting, St. Louis, Paper No. AIAA-81-0248, 1981.
- 3.6 Doss, E. D. and Ahluwalia, R. K., "Three-Dimensional Flow Development in MHD Generators at Part Load," J. Energy, 7, 289 (1983); AIAA Paper 82-0324 (1982).
- 3.7 Fay, J.A., "Hall Effects in a Laminar Boundary Layer of the Hartmann Type," Avco-Everett Research Report 81, 1959.
- 3.8 Girshick, S. L. and Kruger, C. H., "Evidence of Secondary Flow in Faraday MHD Generators," 21st Symposium on Engineering Aspects of Magnetohydrodynamics, Argonne, Illinois, June 1983.
- 3.9 Ishikawa, M. and J. Umoto, "New Approach to Calculation of Three-dimensional Flow in MHD Generators," Proc. 22nd Symposium on Engineering Aspects of Magnetohydrodynamics, Starkville, Mississippi, 1984.

- 3.10 James, R. K. and Kruger, C. H., "Joule Heating Effects in the Electrode Wall Boundary Layer of MHD Generators," AIAA J., 21, 679 (1983).
- 3.11 Liu, B.L., J.T. Lineberry and H.J. Schmidt, "Simplified Three-dimensional Modeling for MHD DCW Channels," J. Energy, 7, 456, 1983.
- 3.12 Maxwell, C.D., D.W. Early and S.T. Demetriades, "Predicted Strength and Influence of MHD-induced Secondary Flows in Recent Experiments," Proc. 23rd Symposium on Engineering Aspects of Magnetohydrodynamics, Somerset, PA., 1985.
- 3.13 Maxwell, C.D., D.M. Markham, S.T. Demetriades, and D.A. Oliver, "Coupled Electrical and Fluid Calculations in the Cross-plane in Linear MHD Generators," Proc. 16th Symposium on Engineering Aspects of Magnetohydrodynamics, Pittsburgh, 1977.
- 3.14 McClaine, A.W., D.W. Swallow and R. Kessler, "Experimental Investigation of Subsonic Combustion-driven MHD Generator Performance, J. Propulsion 1, 263, 1985.
- 3.15 Melling, A. and J.H. Whitelaw, "Turbulent Flow in a Rectangular Duct, J. Fluid Mech. 78, 289, 1976.
- 3.16 Reis, J.C. and C.H. Kruger, "Turbulence Suppression in Combustion-driven Magnetohydrodynamic Channels," accepted for publication in J. Fluid Mech.
- 3.17 Sastry, V.U.K. and C.V.V. Bhadram, "Effect of Hall Currents on the Hydromagnetic Flow in an Annular Channel with a Radial Matnetic Field," Phys. Fluids, 21, 857, 1978.
- 3.18 Sato, H., "The Hall Effect in the Viscous Flow of Ionized Gas Between Parallel Plates Under Transverse Magnetic Field," J. Phys. Soc. Japan, 16, 1427, 1961.
- 3.19 Starr, R.F., L.S. Christensen, G.W. Garrison and G.L. Whitehead, "Preliminary Faraday Performance of a Large Magnetohydrodynamic Generator at High Magnetic Field, J. Energy 6, 163., 1982.
- 3.20 Tani, I., "Steady Flow of Conducting Fluids in Channels Under Transverse Magnetic Fields, with Consideration of Hall Effect," J. Aerospace Sci., 29, 297, 1962.

4.0 PUBLICATIONS AND PRESENTATIONS

To date this program has resulted in the following publications and presentations:

Girshick, S.L. and C.H. Kruger, "Evidence of Secondary Flow in Faraday MHD Generators," 21st Symposium on Engineering Aspects of Magneto-hydrodynamics, Argonne, Illinois (1983).

Kruger, C.H. and S.L. Girshick, "A Review of MHD Boundary Layer Research at Stanford, with Emphasis on Measurements of the Effects of Secondary Flows," 8th International Conference on MHD Electrical Power Generation, Moscow, USSR (1983).

Self, S.A. and L. Eskin, "The Boundary Layers Between Electrodes and a Thermal Plasma," IEEE Trans. Plasma Science, P.S. 11, 279-285 (Dec. 1983).

Girshick, S.L. and C.H. Kruger, "The Transverse Flow Field in an MHD Channel," IEEE International Conference on Plasma Science, May 14-16, 1984, St. Louis.

Girshick, S.L. and C.H. Kruger, "Measurements of Secondary Flow in an MHD Channel," 22nd Symposium on Engineering Aspects of MHD, Mississippi State University, Mississippi, June 26-28, 1984.

Girshick, S.L. and C.H. Kruger, "Experimental Study of Secondary Flow in a Magnetohydrodynamic Channel," accepted for publication in J. Fluid Mech.

Girshick, S.L. and C.H. Kruger, "Experimental Study of Secondary Flow in an MHD Channel," 23rd Symposium on Engineering Aspects of MHD, Somerset, Pennsylvania (June 1983).

Reis, J.C. and C.H. Kruger, "Turbulence Suppression in Combustion-Driven Magnetohydrodynamic Channels," accepted for publication in Journal of Fluid Mechanics.

Self, S.A. and L.D. Eskin, "Plasma-Sheath Structure for an Electrode Contacting an Isothermal Plasma: I. Formulation and Quasi-Neutral Solution," presented at the 38th Gaseous Electronics Conference, Monterey, CA., October 1985.

Eskin, L.D. and S.A. Self, "Plasma-Sheath Structure for an Electrode Contacting an Isothermal Plasma: II. An Electrically Isolated (Floating) Electrode," presented at the 38th Gaseous Electronics Conference, Monterey, CA., October 1985.

Jaffe, S.M., M. Mitchner and S.A. Self, "Electron-Ion Recombination Rates in an Atmospheric Pressure Plasma," presented at the 38th Annual Gaseous Electronics Conference, Monterey, CA., October 1985.

Eskin, L.D. and S.A. Self, "Plasma-Sheath Structure for an Electrode Contacting an Isothermal Plasma: I. Formulation and Quasi-Neutral Solution," submitted to Phys. Fluids.

Eskin, L.D. and S.A. Self, "Plasma-Sheath Structure for an Electrode Contacting an Isothermal Plasma: II. An Electrically Isolated (Floating) Electrode," submitted to Phys. Fluids.

Kruger, C.H., "Boundary Layer Phenomena in MHD Generators," 3rd US/Japan Symposium on MHD, Hakone, Japan (August 1985).

5.0 PERSONNEL

The following personnel contributed to this report.

- Charles H. Kruger Professor and Chairman, Department of Mechanical Engineering (Ph.D. Mechanical Engineering, minor Physics, Massachusetts Institute of Technology 1960. Thesis: "The Axial Flow Compressor in the Free Molecule Range")
- Morton Mitchner Professor, Department of Mechanical Engineering (Ph.D. Physics, Harvard University 1952. Thesis: "The Propagation of Turbulence into a Laminar Boundary Layer")
- Sidney A. Self Professor (Research), Department of Mechanical Engineering (Ph.D. Physics, London University 1965. Thesis: "Radio-Frequency Interaction in a Beam-Generated Plasma System")
- Leo D. Eskin Research Assistant, High Temperature Gasdynamics Laboratory, Department of Mechanical Engineering. (M.S. Mechanical Engineering, Virginia Polytechnic Institute and State University 1981. Thesis: "Application of the Monte Carlo Method to the Transient Thermal Modeling of a Diffuse-Specular Radiometer Cavity")
- Stephen M. Jaffe Research Assistant, High Temperature Gasdynamics Laboratory, Department of Mechanical Engineering (M.S. Mechanical Engineering, Stanford University 1983)
- Douglas W. Johnson Research Assistant, High Temperature Gasdynamics Laboratory, Department of Mechanical Engineering (B.S. ME, 1984), University of California, Davis.

END

DTIC

8-86